













Spectroscopic Analysis Tool for intEgraL fieLd unIt daTacubEs (SATELLITE): Case studies of NGC 7009 and NGC 6778 with MUSE

S. Akras¹ *, H. Monteiro² , J. R. Walsh³ , J. García-Rojas^{4,5} , I. Aleman² ,
 H. Boffin³ , P. Boumis¹ , A. Chiotellis¹ , R. M. L. Corradi^{5,6} , D. R. Gonçalves⁷,
 L. A. Gutiérrez-Soto⁸ , D. Jones^{4,5} , C. Morisset⁹ , X. Papanikolaou¹⁰

¹Institute for Astronomy, Astrophysics, Space Application & Remote Sensing, National Observatory Athens, GR-15236, Athens, Greece

²Instituto de Física e Química, Universidade Federal de Itajubá, Av. BPS 1303, Pinheirinho, 37500-903, Itajubá, MG, Brazil

³European Southern Observatory, Karl-Schwarzschild Strasse 2, D-85748 Garching, Germany

⁴Instituto de Astrofísica de Canarias (IAC), E-38205 La Laguna, Tenerife, Spain

⁵Departamento de Astrofísica, Universidad de La Laguna, E38206, La Laguna, Tenerife, Spain

⁶GRANTECAN, Cuesta de San José s/n, E-38712 Breña Baja, La Palma, Spain

⁷Observatório do Valongo, Universidade Federal do Rio de Janeiro, Ladeira Pedro Antonio 43, Rio de Janeiro 20080-090, Brazil

⁸Departamento de Astronomia, IAG, Universidade de São Paulo, Rua do Matão, 1226, 05509-900, São Paulo, Brazil

⁹Universidad Nacional Autónoma de México, Instituto de Astronomía, AP 106, Ensenada, 22800, BC, Mexico

¹⁰Dionysos Satellite Observatory (DSO), School of Rural, Surveying and Geoinformatics Engineering, National Technical University of Athens, Iroon Polytechniou Str. 9, 15780 Zografou, Greece

Accepted XXX. Received YYY; in original form ZZZ

ABSTRACT

Integral field spectroscopy (IFS) provides a unique capability to spectroscopically study extended sources over a 2D field of view, but it also requires new techniques and tools. In this paper, we present an automatic code, Spectroscopic Analysis Tool for intEgraL fieLd unIt daTacubEs, SATELLITE, designed to fully explore such capability in the characterization of extended objects, such as planetary nebulae, H II regions, galaxies, etc. SATELLITE carries out 1D and 2D spectroscopic analysis through a number of pseudo-slits that simulate slit spectrometry, as well as emission line imaging. The 1D analysis permits direct comparison of the integral field unit (IFU) data with previous studies based on long-slit spectroscopy, while the 2D analysis allows the exploration of physical properties in both spatial directions. Interstellar extinction, electron temperatures and densities, ionic abundances from collisionally excited lines, total elemental abundances and ionization correction factors are computed employing the PYNEB package. A Monte Carlo approach is implemented in the code to compute the uncertainties for all the physical parameters. SATELLITE provides a powerful tool to extract physical information from IFS observations in an automatic and user configurable way. The capabilities and performance of SATELLITE are demonstrated by means of a comparison between the results obtained from the Multi Unit Spectroscopic Explorer (MUSE) data of the planetary nebula NGC 7009 with the results obtained from long-slit and IFU data available in the literature. The SATELLITE characterization of NGC 6778 based on MUSE data is also presented.

Key words: planetary nebulae: general – planetary nebulae: individual: NGC 7009, NGC 6778 – H II regions – ISM: abundances – methods: numerical; Astronomical instrumentation, methods, and techniques

1 INTRODUCTION

Recent advances in integral field spectroscopy (IFS) have promoted a huge growth in imaging spectroscopy, demanding new approaches to the study of extended and resolved objects. Over the last two decades several integral field units (IFU) have been built covering mainly optical and infrared wavelengths, with diverse characteristics, such as field of view, wavelength coverage, spatial resolution, resolving

power (see conference review on IFS, [Allington-Smith et al. 2006](#); [Mediavilla et al. 2011](#)).

IFS provides data in 3 dimensions (2 spatial and 1 spectral) or, equivalently, a cube of data where each wavelength element corresponds to a spectral image. These data cubes make possible the simultaneous spectroscopic analysis of extended objects (e.g. galaxies, H II regions, planetary nebulae) in both spatial directions providing the spatial distribution of emission lines fluxes, line ratios and the nebular physical parameters (e.g. extinction, electron temperature and density (T_e , N_e), abundances), a task that is very time-consuming with traditional long-slit spectroscopy techniques (e.g. [Monteiro et al.](#)

* E-mail: stavrosakras@gmail.com

2004, 2005; Phillips et al. 2010; Leal-Ferreira et al. 2011) or CCD imaging spectroscopy (e.g. Jacoby et al. 1987; Lame & Pogge 1994, 1996).

These advances have boosted the number of works devoted to spatially resolved studies of planetary nebulae (PNe) using IFS over the last decade; some representative examples of these studies are, e. g. Tsamis et al. (2008), Monteiro et al. (2013), Ali et al. (2016), Walsh et al. (2016), Walsh et al. (2018), Ali & Dopita (2019), Monreal-Ibero & Walsh (2020), Akras et al. (2020a), and García-Rojas et al. (2022).

The vast majority of spectroscopic studies of extended objects have been performed employing the traditional long-slit spectroscopy. As a consequence, spectroscopic data are available only for specific regions where the slits or apertures were placed. Moreover, diagnostic diagrams such as BPT (Baldwin et al. 1981), VO (Veilleux & Osterbrock 1987) and STB (Sabbadin et al. 1977), built to distinguish AGN, LINERs, and Seyfert galaxies or PNe, SNRs and H II regions are also based on 1D long-slit data as well as simulations from 1D models such as CLOUDY (Ferland et al. 2013, 2017) and MAPPINGS (Sutherland & Dopita 2017; Sutherland et al. 2018).

From IFU data, besides the unique 2D spectroscopic analysis, it is also possible to perform 1D analysis by simulating slit apertures (hereafter “pseudo-slits”). This is essential to acquire results that can be properly compared with those from long-slit studies present in the literature. For instance, it has already been pointed out that a spaxel-by-spaxel analysis of emission line ratios of extended sources from IFUs is not recommended for a straightforward comparison with integrated long-slit spectra and the resultant diagnostic diagrams (Ercolano et al. 2012; Morisset 2018; Akras et al. 2020a).

In this paper, we present a newly developed automatic code that performs a full spectroscopic analysis of extended sources using IFS data, namely “Spectroscopic Analysis Tool for intEgraL fieLd unIt daTacubEs (SATELLITE)”. The novelty of this tool is that it provides an 1D spectroscopic analysis through pseudo-slits and 2D analysis through maps. The former will allow to properly compare the results obtained from IFUs with those from previous 1D long-slit spectroscopy while the latter will allow to explore the extended sources in both spatial directions. A brief presentation of the capabilities of SATELLITE is presented in Akras et al. (2020a) using VIMOS IFS data of the PN Abell 14.

The paper is organized as follows. In Section 2, we present the four modules of the SATELLITE code available in the current version namely: (I) *rotation analysis*, (II) *radial analysis*, (III) *specific slits analysis* and (IV) *2D analysis*. In Sections 3 and 4, we apply the SATELLITE code to the Multi Unit Spectroscopic Explorer (MUSE) Science Verification data of the PN NGC 7009, as well as the data from program 097.D-0241(A) (PI: Corradi). A comparison between SATELLITE’s results and those from Walsh et al. (2018) is presented as well as the outcomes from the two MUSE datacubes. In Section 5, we apply the SATELLITE code to the MUSE data of NGC 6778 and perform the 1D and 2D spectroscopic characterization of the nebula. The results of this work as well as the potential upgrades to future versions of the SATELLITE code are discussed in Section 6.

2 THE SATELLITE CODE

The Spectroscopic Analysis Tool for intEgraL fieLd unIt daTacubEs (SATELLITE) is a newly developed PYTHON 3 code that performs a number of spectroscopic analyses on IFU data. As input, SATELLITE

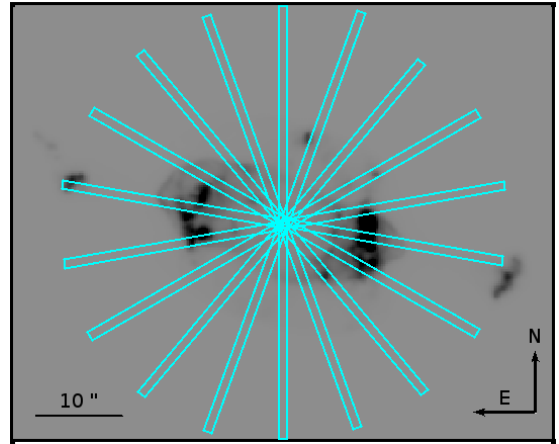


Figure 1. Illustrative example of pseudo-slits positions in NGC 7009 overlaid on the [N II] 6584 Å image for the rotation analysis module. The width, length, initial, final and step angle are provided by the user. The size of the image is 62×50 arcsec.

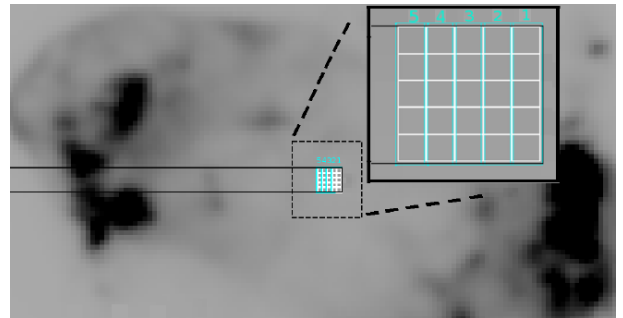


Figure 2. Illustrative example of the *radial analysis* module for the PA=90 degrees pseudo-slit in NGC 7009 overlaid on the [N II] 6584 Å image. The inset image shows a zoomed-in of the pseudo-slit. The boxes correspond to the spaxels of the IFU. The fluxes of the spaxels in each numbered column/row are summed up to get the total flux for each column/row within the width of the pseudo-slit or equivalently to the distance from the central star taking into account the pixel scale of the IFU.

uses the flux maps of several emission lines usually detected in galaxies, H II regions and PNe¹, extracted from IFU datacubes.

SATELLITE simulates pseudo-slit spectra by summing up the values of each individual spaxel (the unit of the IFU) within the specific region defined by the width and length of the pseudo-slits provided by the user. Note that the pseudo-slits are built considering full-size spaxels and no partially covered ones.

To exclude values from problematic spaxels or with low signal-to-noise (S/N) ratio, two criteria must be satisfied by each spaxel: (i) $F(H\alpha) > 0$, $F(H\beta) > 0$ and (ii) $F(H\alpha) > 2.85 * F(H\beta)$, to avoid unrealistic values for the interstellar extinction coefficient ($c(H\beta)$)².

For all the modules, SATELLITE³ first calculates $c(H\beta)$ consider-

¹ The analysis of weak collisionally excited lines and recombination lines from O or N is not implemented yet.

² Negative $c(H\beta)$ values are still possible especially in the halo of PNe due to scattering process. Walsh et al. (2018) reported negative $c(H\beta)$ values at the halo of NGC 7009 after applying the Voronoi tessellation method. This technique is not yet implemented in the SATELLITE code.

³ SATELLITE is available to the GitHub website with its proper documentation and example <https://github.com/StavrosAkras/SATELLITE.git>.

ing an extinction curve law selected by the user among the options in the PYNEB package version 1.1.15 (Luridiana et al. 2015). Then it computes the physical parameters of the ionized nebula such as T_e and N_e , ionic abundances, ionization correction factors (ICFs), total elemental abundances and abundance ratios, employing the PYNEB package. In this work, we used the default atomic databases in the PYNEB package (see Morisset et al. 2020). The diagnostic lines for the determination of T_e and N_e as well as the values applied for the ionic abundances determinations are set by the user from a list of diagnostics. The uncertainties of the physical parameters are computed following Monte Carlo simulations. The number of random spectra (hereafter replicate spectra) is chosen by the user and they are generated considering a Gaussian distribution centred at a reference spectrum (i.e. line intensities) with a sigma equal to the uncertainty of each line intensity computed from the provided error maps⁴. Then, all the physical parameters are computed for each replicate spectrum and the resultant standard deviation of the distribution of each parameter is considered to be the final uncertainty provided by the SATELLITE code. Besides the calculations of nebular physical parameters for the pseudo-slits, SATELLITE also provides scatter plots, emission line diagnostic diagrams, histograms and 2D maps for all nebular parameter. The modules of SATELLITE are described below.

2.1 Rotation analysis module

This module deals with the spectroscopic analysis of an extended source from a number of pseudo-slits placed radially across half of the nebula with position angles (PAs) from 0 to 360 degrees (Fig. 1). SATELLITE first rotates all raw images (line flux maps) and then generates new images from which it computes the fluxes summing up the values of each individual pixel with the pseudo-slit. The pseudo-slits are always in vertical direction (up-and-down orientation).

PA=0 degrees corresponds to a pseudo-slit in vertical orientation on the map and increases as the pseudo-slit rotates in the anti-clockwise direction. If the IFU data and the line flux maps are oriented such that North is up and East is left, the PA of the pseudo-slits in the SATELLITE's frame coincides with the slits' PA on-sky values (PA=0 degrees in the North-South direction and increases rotating East from North). The initial, final and step angles of the position angle as well as the width and the length of the pseudo-slits are given by the user.

All the line intensities and physical parameters of the nebula are derived for each pseudo-slit. Therefore, this module provides an analysis of nebular gas ($c(\text{H}\beta)$, T_e and N_e , ionic and elemental abundances, ICFs) as functions of slit PA as well as an ASCII file (a multi-column list of data used for the plots) so that users can construct their own plots.

2.2 Radial analysis module

The *radial analysis* module computes the emission line fluxes along a specific pseudo-slit as a function of the distance from the geometric center and/or the ionizing source (e.g. central star). The characteristics of this pseudo-slit (PA, width and length) are free parameters provided by the user. SATELLITE calculates the line fluxes summing up the values of the individual spaxels in one column/row enclosed by the pseudo-slit (Fig. 2) and then all the physical parameters of

⁴ An additional error can also be considered for each emission line as a percentage of the line flux for all the systematic uncertainties. This error is a free parameter in the code and it is given by the user.

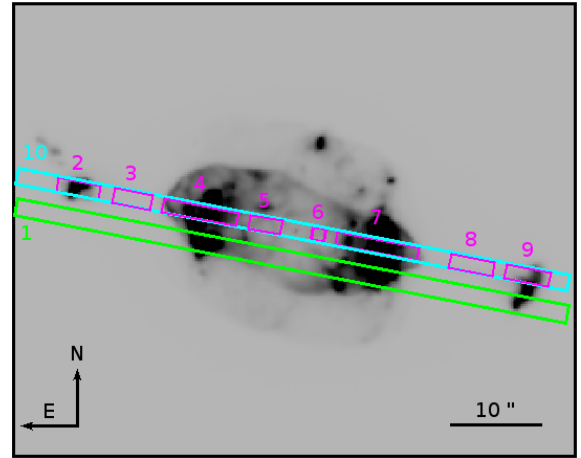


Figure 3. Ten selected regions in NGC 7009 overlaid on the [N II] 6584 Å image. The position of the centre (x, y coordinates), position angle, width and length of the slits are free parameters provided by the user. Slits 1 and 10 represent the slits position from Fang & Liu (2011) and Gonçalves et al. (2003), respectively. Numbered regions from 2 to 9 correspond to the sub-structures of knots and jet-like, or sub-regions of rims defined in Gonçalves et al. (2003). The size of the image is 62×50 arcsec.

the nebula at each column/row). Scatter plots for each parameter as a function of the distance taking into account the pixel scale of the IFU are provided as well as an ascii file with the data. The distance from the central star at which each emission line shows a peak is also determined. The emission lines for this task are also chosen by the user. Overall, the *radial analysis* module makes possible the study of nebular parameters and line ratios as a function of the distance from the central ionising source of the nebula.

2.3 Specific slits analysis module

The *specific slits analysis* module performs a full spectroscopic analysis for 10 (default number in SATELLITE v1.3) distinct regions that can be configured so as to study specific features/regions that possess distinctive morphological or physical properties, such as lobes, ansae, low-ionization structures (LISs), rim, etc. in PNe for a direct comparison with the results from long-slit studies.

Line intensities and physical parameters are calculated for each specific region defined by the pseudo-slits summing up all the spaxels values. The exact position/centre, PA, width and length of the pseudo-slits are not necessarily the same and are provided by the user. Fig. 3 displays the 10 selected regions for the analysis of NGC 7009 overlaid on its [N II] 6584 Å image.

2.4 2D analysis module

The fourth SATELLITE module performs the full 2D spectroscopic analysis. This module calculates the line intensities and physical parameters in each spaxel and only for those that satisfy the aforementioned criteria. The principal outputs of this module are 2D maps of line ratios, nebular parameters, ionic and total elemental abundances as well as the corresponding histograms of their distributions. Moreover, the mean values, standard deviations and percentiles of 5%, 25% (Q1), 50% (median), 75% (Q3), 95% are also calculated for all the line ratios and nebular parameters.

A number of emission line diagnostic diagrams (including the classical BPT/VO, STB) selected by the user among a pre-defined

Table 1. Comparison between SATELLITE and Walsh et al. (2018) results obtained from the NGC 7009 Science Verification MUSE data. Flux maps used for this comparison were those extracted by Walsh et al. (2018).

Parameter	SATELLITE	SD [†]	Walsh et al. (2018)	SD	Log(ratio)	SD	# of spaxels
c(H β)	0.105	0.065	0.122	0.041	-0.022	0.165	28070
Te(SIII6312_9069)_Ne(CIII5517_5538)	9166	301	9159	326	0.0005	0.0024	17305
Ne(CIII5517_5538)_Te(SIII6312_9069)	3609	2037	3547	2476	0.0001	0.0015	17305
log(He I 5876/H α)	-1.264	0.035	-1.270	0.031	-0.004	0.002	35876
log(He II 5412/H β)	-2.443	0.484	-2.425	0.484	0.004	0.001	14427
log([N II] 6583/H α)	-1.465	0.379	-1.447	0.336	0.0001	0.0014	39302
log([O I] 6300/H α)	-2.953	0.833	-2.880	0.863	-0.0009	0.0007	11720
log([O III] 4959/H β)	0.666	0.080	0.699	0.078	-0.0025	0.0016	40724
He ⁺ (5876)/H ⁺	0.105	0.008	0.102 ^{††}	0.009	0.013	0.012	16516
He ⁺ (6678)/H ⁺	0.100	0.008	0.102 ^{††}	0.009	-0.010	0.010	16516
He ⁺⁺ (5412)/H ⁺	0.007	0.008	0.007	0.008	-0.001	0.003	14042
N ⁺ (6548)/H ⁺ (10 ⁻⁶)	5.688	14.499	5.875 ^{††}	14.66	-0.017	0.014	17304
N ⁺ (6584)/H ⁺ (10 ⁻⁶)	5.789	14.752	5.875 ^{††}	14.66	-0.009	0.014	17304
O ⁺ (7320)/H ⁺ (10 ⁻⁵)	3.491	3.384	3.068	2.703	0.060	0.031	17296
O ⁺ (7330)/H ⁺ (10 ⁻⁵)	3.728	3.351	3.068	2.703	0.090	0.028	17283
O ⁺⁺ (4959)/H ⁺ (10 ⁻⁴)	5.659	0.688	5.992	0.765	-0.024	0.011	17253
S ⁺ (6716)/H ⁺ (10 ⁻⁷)	3.176	6.882	2.977 ^{††}	6.101	0.014	0.055	17301
S ⁺ (6731)/H ⁺ (10 ⁻⁷)	2.927	6.102	2.977 ^{††}	6.101	-0.010	0.014	17305
S ⁺⁺ (6312)/H ⁺ (10 ⁻⁶)	4.490	1.548	4.616	1.618	-0.012	0.017	17305
Cl ⁺⁺ (5517)/H ⁺ (10 ⁻⁷)	0.998	0.240	1.019	0.248	-0.009	0.012	17305
Ar ⁺⁺ (7136)/H ⁺ (10 ⁻⁶)	1.645	0.337	1.837	0.384	-0.048	0.015	17305

[†] Standard Deviation from the whole map. ^{††} These are average ionic abundances from both ions. (Walsh et al. 2018) data are available in the The Strasbourg astronomical Data Center (<http://cdsarc.u-strasbg.fr/viz-bin/qcat?J/A+A/620/A169>)

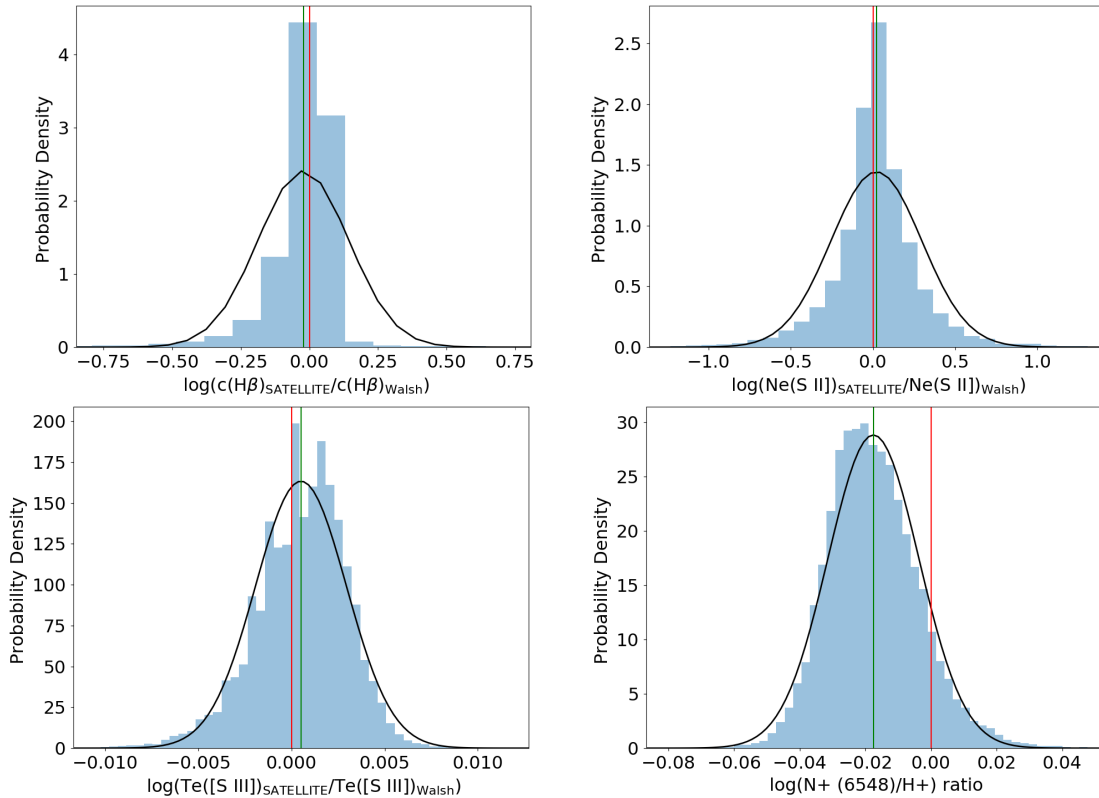


Figure 4. Comparison distributions of the $\log(c(\text{H}\beta)_{\text{satellite}} / c(\text{H}\beta)_{\text{Walsh}})$ (upper, left panel), $\log(N_e[\text{S II}]_{\text{satellite}} / N_e[\text{S II}]_{\text{Walsh}})$ (upper right panel), $\log(T_e[\text{S III}]_{\text{satellite}} / T_e[\text{S III}]_{\text{Walsh}})$ (lower left panel) and $\log(N^+(6548)/H^+)$ ratios (lower right panel) between the results obtained with SATELLITE and computed by Walsh et al. (2018). Red and green vertical lines indicate the zero value and the peak of each distribution. The black lines represent the probability density functions of the data.

list in SATELLITE are also generated and provided. There is an option to plot the values obtained from the *rotation analysis* and *specific slits analysis* modules and the *2D analysis* from all spaxels on the same diagnostic diagrams.

The comparison of the emission line ratios from individual spaxel line ratios with the ratios obtained from integrated slits is crucial for the study of extended sources such as galaxies, H II regions and PNe and the interpretation of the excitation mechanisms (Ercolano et al. 2012; Morisset 2018; Akras et al. 2020a). Moreover, the available Ionization Correction Factors (ICFs) formulae for the computation of the total elemental abundances can be made only for 1D spectra rather than for each individual spaxel. The ionization structure of PNe is strongly dependent on the distance from the UV-source (e.g. PN central star) which can lead to misleading 2D abundances estimations.

3 CASE STUDY OF NGC 7009 WITH THE SCIENCE VERIFICATION MUSE DATA

In order to illustrate further and assess the numerical tools provided by SATELLITE, we use as a case study the planetary nebula NGC 7009, also known as the Saturn nebula, and it is among the most extensively studied PNe. Observations covering a large portion of the electromagnetic spectrum are available. Its high surface brightness has made possible various thorough studies using both imaging and spectroscopic data (e.g. Lame & Pogge 1996; Guerrero et al. 2002; Rubin et al. 2002; Gonçalves et al. 2003; Sabbadin et al. 2004; Gonçalves et al. 2006; Rodríguez & Gómez 2007; Steffen et al. 2009; Phillips et al. 2010; Fang & Liu 2011, 2013; Akras et al. 2020b). As a consequence, NGC 7009 was also an ideal object for MUSE (Bacon et al. 2010) Science Verification (SV) phase, and the first results from these data have been published by Walsh et al. (2016, 2018).

The same emission line flux maps extracted from the SV MUSE datacube (Walsh et al. 2018) available in VizieR On-line Data Catalog (J/ApJ/889/49) are used to test the performance of the SATELLITE code and compare its outputs with those from Walsh et al. (2018) as well as the long-slit spectra from Fang & Liu (2011) and Gonçalves et al. (2003). The resulting maps from SATELLITE and Walsh et al. (2018) are first compared through a spaxel-by-spaxel approach. For this exercise, the same Galactic extinction law from Seaton (1979) was considered for the spectroscopic analysis with SATELLITE. Table 1 lists the mean values and standard deviations for the maps of some physical parameters, logarithmic line ratios and ionic abundances. For the majority of the parameters the difference is found to be less than 5 percent with comparable dispersion (similar standard deviations). Note that the current version of the SATELLITE code does not correct for the contribution of recombination lines which may not be negligible, especially in PNe with relatively large abundance discrepancy factors between optical recombination lines and collisionally excited lines, where this correction can be extremely problematic (see Gómez-Llanos et al. 2020). This explains the difference in the abundance of singly ionized Oxygen between SATELLITE and (Walsh et al. 2018) as the O^{++} recombination contribution results in 30 percent higher O^+/H^+ . The $T_e[S\text{ III}]$ and $N_e[Cl\text{ III}]$ diagnostic line were considered for all the calculations in order to replicate the exact outputs from Walsh et al. (2018).

Fig. 4 displays some representative examples of comparison histograms of different parameters and abundance ratios obtained from the SATELLITE code and Walsh et al. (2018). Probability density functions are also shown (black line) with peaks very close to zero, which verifies the consistency and robustness of the code.

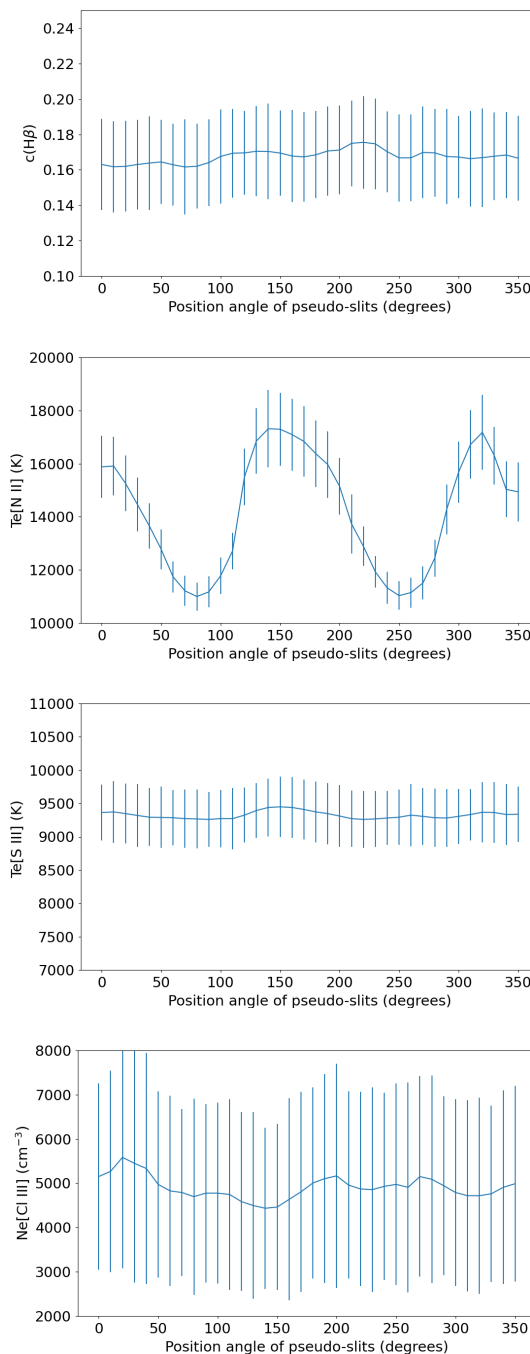


Figure 5. $c(H\beta)$ (first panel), $T_e[N\text{ III}]$ (second panel), $T_e[S\text{ III}]$ (third panel), and $N_e[Cl\text{ III}]$ (fourth panel) versus the position angle of the pseudo-slits. PA=0 degrees corresponds to a pseudo-slit oriented north-south and increases rotating to the east.

3.1 Rotation analysis module

The complex morphology of NGC 7009 composed of the ellipsoidal main nebula, several sets of outer shells, loops, jet-like features and pairs of LISs, make it an ideal nebula for demonstrative purposes of SATELLITE's capabilities and the *rotation analysis* module. The position angle of the pseudo-slits varies from 0 to 360 with a step of 10 degrees. Fig. 5 illustrates the variation of $c(H\beta)$ (first panel),

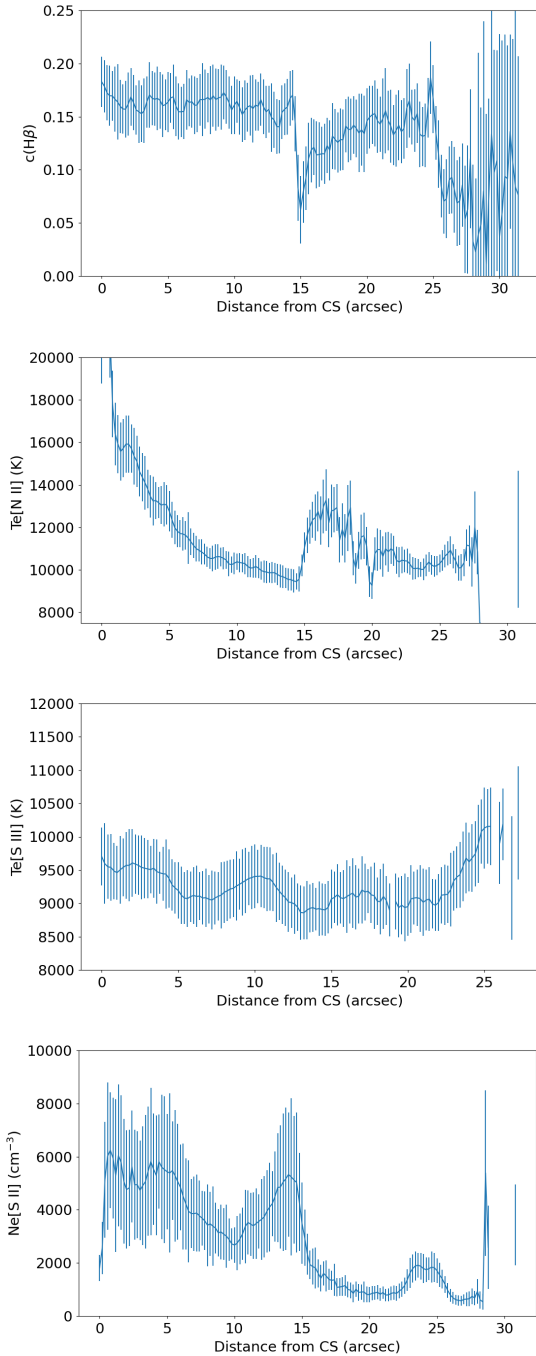


Figure 6. $c(H\beta)$ (first panel), $T_e[N\ II]$ (second panel), $T_e[S\ III]$ (third panel) and $N_e[S\ II]$ (fourth panel) as a function of the distance from the central star (in arcsec) in a pseudo-slit at PA=79 degrees.

$T_e[N\ II]$ (second panel), $T_e[S\ III]$ (third panel) and $N_e[Cl\ III]$ (forth panel) as functions of the PA.

$c(H\beta)$ slightly varies with the PA from 0.16 to 0.17 but it can be considered constant within the uncertainties. Thus, no divergence along the direction of the jet-like/LISs is found. $T_e[N\ II]$ shows strong variation with the PA between 10000 K up to 17000 K. However, this variation shall not be considered real. It is associated with the high values in the central region of the nebula reported by [Walsh et al. \(2018\)](#). On the other hand, $T_e[S\ III]$ displays a constant value

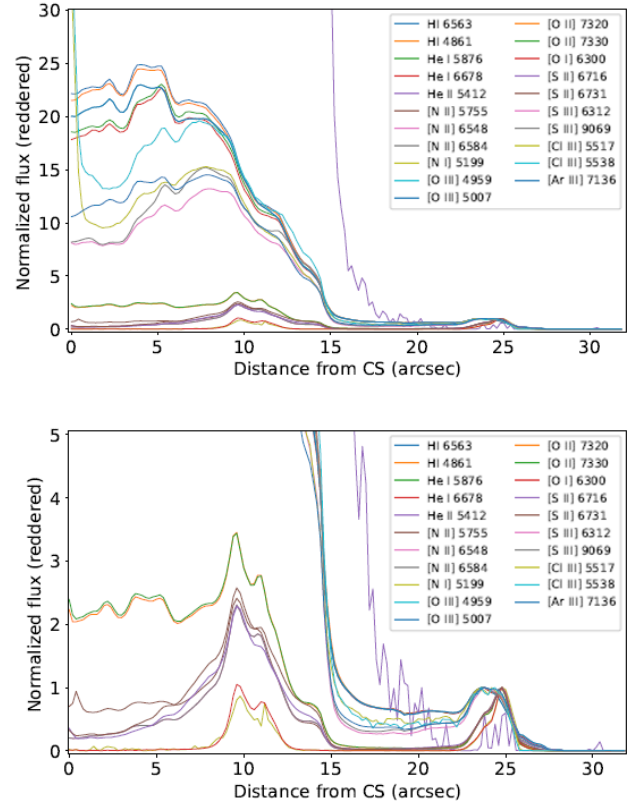


Figure 7. Radial distribution of emission lines normalized to 1. The normalization is made at the peak values for distances >20 arcsec. Lower panel zooms in to better illustrate the distribution of weaker lines.

of ~ 9400 K, being 2000 K lower than the values estimated by [Fang & Liu \(2011\)](#) despite the good agreement in line intensities. It should be noted that [Fang & Liu \(2011\)](#) measured T_e from the $T_e[S\ III]$ 6312/(9069+9530) line ratio while SATELLITE considers the $T_e[S\ III]$ 6312/9069 ratio⁵. From the reported intensities of the nebular [S III] lines by [Fang & Liu \(2011\)](#), [S III] $\lambda 9530$ line is likely dimmed by atmospheric absorption bands (the [S III] $\lambda 9531/\lambda 9069$ ratio is 1.88 in contrast with the expected theoretical value of 2.48 from the transition probabilities of [Mendoza & Zeippen 1982](#)) resulting in higher temperature. This disagreement in $T_e[S\ III]$ is also responsible for the difference in the ionic abundances showed in Table 1. Nevertheless, the results from the Cor MUSE data ((097.D-0241(A), PI: R. L. M. Corradi; see Section 4) agree with the results from the earlier MUSE SV data. $N_e[Cl\ III]$ can also be considered constant within the uncertainties. To avoid possible false variations in the chemical abundances of the nebula, $T_e[S\ III]$ and $N_e[Cl\ III]$ were used to derive the chemical abundances and replicate the results from [Walsh et al. \(2018\)](#).

3.2 Radial analysis module

In Fig. 6, we present the variation of $c(H\beta)$ (first panel), $T_e[N\ II]$ (second panel), $T_e[S\ III]$ (third panel) and $N_e[S\ II]$ (fourth panel) as functions of the distance from the central star for a slit at PA=79 degrees

⁵ The location of the telluric features in the MUSE spectra of NGC 7009 (corrected for the motion of the Sun and Earth) was also verified without evidence for telluric features around 9069Å that could be responsible for the diminish of the line.

Table 2. Distances of the outer emission line peak from the central star in a pseudo-slit at PA=79 degrees.

Line	Distance [†] (arcsec)	Line	Distance (arcsec)
H I 4861 Å	23.6	[N II] 6584 Å	24.8
[O III] 4959 Å	23.8	H I 6563 Å	23.6
[N I] 5199 Å	24.8	[N II] 6548 Å	24.8
He II 5412 Å	20.2	He I 6678 Å	23.8
[Cl III] 5517 Å	24.2	[S II] 6717 Å	24.8
[Cl III] 5538 Å	24.4	[S II] 6731 Å	24.8
[N II] 5755 Å	24.2	[Ar III] 7136 Å	24.8
He I 5876 Å	23.6	[O II] 7320 Å	24.8
[O I] 6300 Å	24.8	[O II] 7330 Å	24.8
[S III] 6312 Å	23.8	[S III] 9069 Å	23.8

[†] The spatial resolution of MUSE maps is 0.2 arcsec.

(along the direction of the eastern jet/knot). $c(H\beta)$ is nearly flat (~ 0.16) for a distance up to 14-15 arcsec from the central star where it drops sharply to 0.06. This position corresponds exactly to the end of the ellipsoidal structure and the beginning of the jet-like structure. This drop in $c(H\beta)$ is also highlighted in Walsh et al. (2016). Then it gradually increases from 0.06 up to 0.16 at the distance of 25 arcsec. Above that distance, the diffuse and weaker $H\alpha$ and $H\beta$ emission lines from the halo lead to large uncertainties and no robust results can be extracted.

[N II] diagnostic lines yield a very high electron temperature in the inner nebula (< 8 arcsec), which corresponds to the high value reported by Walsh et al. (2018), and at a distance of 15-17 arcsec from the central star, where there is a peak of ~ 14000 K. It is worth noting the radial distribution of $T_e[S III]$. For distances up to ~ 22 arcsec, $T_e[S III]$ is nearly constant (~ 9200 K) and then it slightly increases to ~ 10500 K. This increase of $T_e[S III]$ may be associated with a change of ionization and physical conditions across the LIS, shock heating process or photoelectric heating by dust. Intriguingly, the model of the nebula from Sabbadin et al. (2004) shows an increasing $T_e[S III]$ with the distance from the central star ending with a bump at the position of the LISs (see their fig. 10). As for N_e , both diagnostics ([S II] and [Cl III]) display a very similar radial distribution with clear bumps at $11 < r < 15$ arcsec and $23 < r < 26$ arcsec the exact positions of K2/K4 and K1/K4 sub-structures, respectively (see Gonçalves et al. 2003).

Besides the radial distribution of the line fluxes as a function of the distance from the central star, the *radial analysis* module also provides the distance from the central star in which each line peaks for a specific region in the nebula defined by the user. For the case of NGC 7009 (Fig. 7), the radial distributions of emission lines are normalized to unity for distances > 20 arcsec (focused at the NE-LISs). The moderate/high ionization lines (e.g. [O III], [Ar III]) as well as the recombination lines $H\alpha$ and $H\beta$ are brighter in the inner nebula and drops outwards from 10 arcsec from the central star and peak again at the position of the knots ($r=23-26$ arcsec). On the other hand, the low ionization lines show a first peak at the position of the K2(K3) sub-structures around 10 arcsec and a second one at the position of the K1(K4) knots (Gonçalves et al. 2003).

Note that the moderate/high and low-ionization lines peak at difference radial distances from the central star (see lower panel of Fig. 7). In Table 2, we list the distance from the central star where each line shows an augmentation at the position of ~ 25 arcsec (K1 knot, Gonçalves et al. 2003) and a clear stratification is found. In

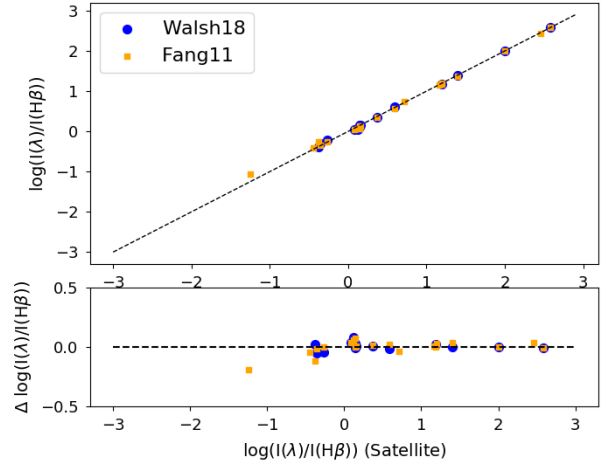


Figure 8. Comparison of the line ratios relative to $H\beta=100$ for the pseudo-slit at PA=79 degrees along the major axis of NGC 7009 studied by Fang & Liu (2011). The line ratios from Fang & Liu (2011) (labelled as Fang 11) and those reported by (Walsh et al. 2018, labelled as Walsh 18) are compared to the line ratios from the MUSE data using SATELLITE.

particular, the low-ionization lines (e.g., [N II], [O II], [S II], etc.) peak at a distance of 24.8 arcsec, while the moderate/high ionization lines (e.g., [O III], [S III], [Cl III], etc.) display a peak closer to the central star by 0.6-1 arcsec (Fig. 7).

3.3 Specific slits analysis module

For a direct comparison of the pseudo-slits spectra with previous long-slit spectroscopic data of NGC 7009 (Gonçalves et al. 2003; Fang & Liu 2011), we employed the *specific slits* module to replicate the observations. Line intensities are computed by SATELLITE for a number of slit positions/regions (Fig. 3, Table 3). Fig. 8 displays the comparison between the line intensities computed from SATELLITE and those from Walsh et al. (2018) and Fang & Liu (2011) for the slit 1. For the interstellar extinction, we consider the same laws used in the studies above i.e., Howarth (1983) for the pseudo-slit 1 and Cardelli et al. (1989) for the rest of the pseudo-slits. It should also be noted that for the estimation of the ionic and total abundances in this module, $T_e[N II]$ and $N_e[S II]$ were considered for the low-ionization species while $T_e[S III]$ and $N_e[Cl III]$ were used for the moderate/high ionization species.

A reasonable agreement within the uncertainties is found for most of the line intensities as well as for the physical parameters $c(H\beta)$, T_e , N_e and abundances (Table 3). The uncertainties of the physical parameters are calculated considering a Monte Carlo approach and vary from 10 to 30 percent. Higher uncertainties are found for the sub-structures (K or J) because of the small size of the extracted windows (i.e. number of spaxels).

An analysis on the T_e and N_e between the different sub-structures and the entire nebula confirms the systematical lower electronic densities found in LISs compared to the main nebula and comparable electronic temperatures (e.g., Gonçalves et al. 2003, 2009; Akras & Gonçalves 2016). The spectroscopic analysis of the specific regions/sub-structures shows a reasonable agreement with previous studies and verifies the performance of the SATELLITE code. The larger discrepancy is found in $N_e[Cl III]$ for the pseudo-slit 10. We argue

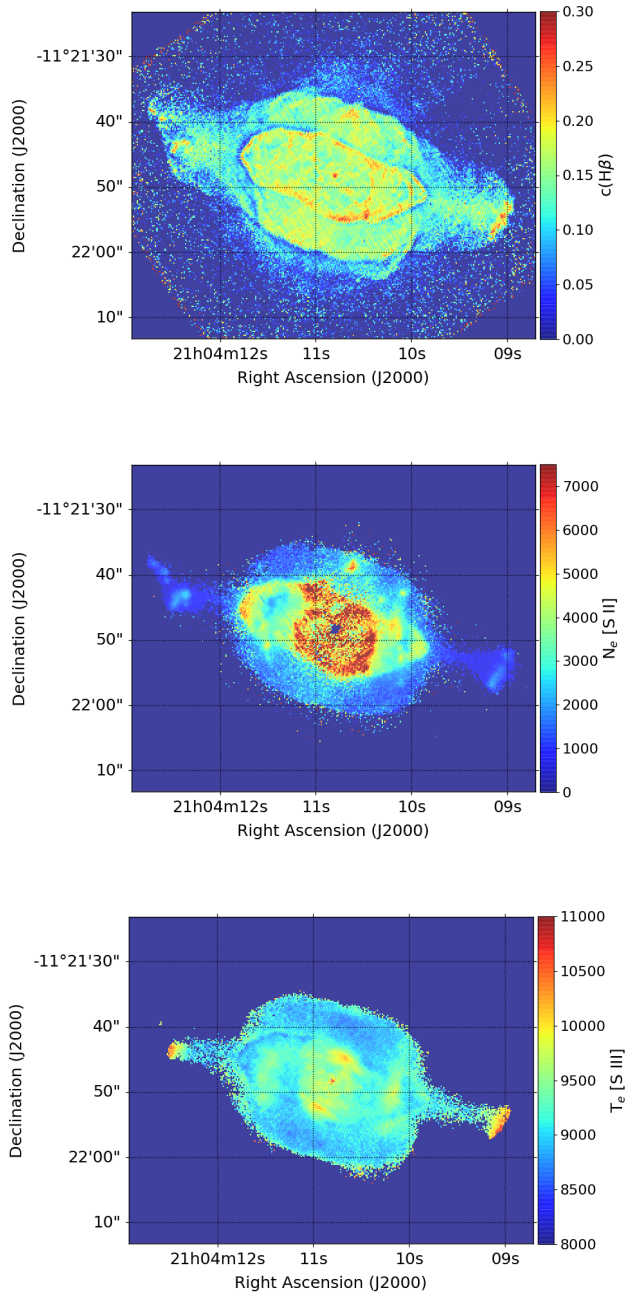


Figure 9. Illustrative output maps of the `SATELLITE` code: $c(H\beta)$ (upper), N_e (middle) and T_e (lower panel).

that the value of 1300 cm^{-3} (Gonçalves et al. 2003) is a typo as the $[\text{Cl III}] \lambda 5517/\lambda 5538$ line ratio is very close to the value computed by `SATELLITE`. Differences in abundances are mainly related to the T_e/N_e diagnostics and the atomic data.

3.4 2D analysis module

Regarding the *2D analysis* module, it allows us to study the entire nebula in both spatial directions simultaneously and explore the distribution of the physical parameters. In Figs 9 and 10, we present as illustrative examples the maps of $c(H\beta)$, T_e , and N_e as well as

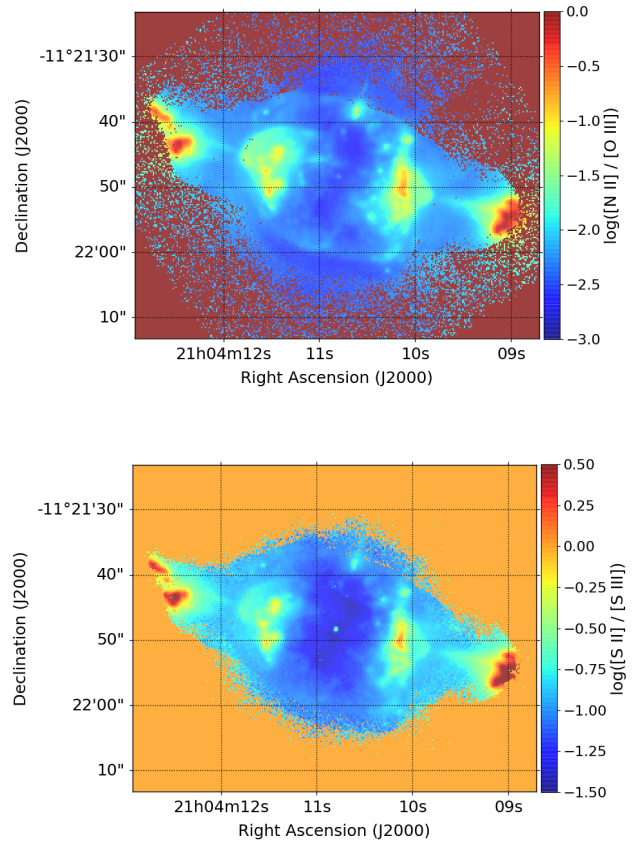


Figure 10. Illustrative output maps of the `SATELLITE` code: $\log([N \text{ II}]/[O \text{ III}])$ (upper) and $\log([S \text{ II}]/[S \text{ III}])$ (lower panel) line ratios.

the $\log([N \text{ II}]/[O \text{ III}])$ and $\log([S \text{ II}]/[S \text{ III}])$ line ratios maps selected from a list of available line ratios. $c(H\beta)$ map displays a filamentary structure in the inner nebula with enhanced extinction at the knots (see also fig. 1 in Walsh et al. 2016). It is evident that $c(H\beta)$ is not smooth throughout the nebula and varies from 0.1 up to 0.3.

Besides the maps, the *2D analysis* module also provides emission line diagnostic diagrams, selected by the user from a predefined list. Fig. 11 illustrates the common diagnostic diagram $\log(H\alpha/[S \text{ II}])$ versus $\log(H\alpha/[N \text{ II}])$. The line ratio values from the individual spaxels are plotted as cyan points, the pseudo-slit spectra from the *rotation analysis* module as purple circles in the main plot or colored circles in the inset plot (color bar corresponds to the PA of the pseudo-slits) and those from the *specific slits analysis* module as yellow diamonds.

The majority of the spaxels as well as some pseudo-slits from the *rotation analysis* and *specific slit analysis* modules (pseudo-slits 1 and 10 that cover the entire nebula from one side to the other) have values up to $\log(H\alpha/[S \text{ II}]) \sim -2.5$ and $\log(H\alpha/[N \text{ II}]) \sim 1.75$ lying outside the 85 percent confidence level ellipse (Riesgo & López 2006). This clearly demonstrates that the regime of PNe in the STB diagnostic diagram should be updated by covering higher $H\alpha/[S \text{ II}]$ and $H\alpha/[N \text{ II}]$ line ratios. The same conclusion has been reached from the prediction of 1D photo-ionization models (see Fig. 5 in Akras et al. 2020a).

Moreover, there is a non-negligible number of spaxels with moderate or even low values ($\log(H\alpha/[S \text{ II}]) < 1.0$ and $\log(H\alpha/[N \text{ II}]) < 0.25$) close to the loci of H II regions and SNRs (Frew & Parker 2010;

Table 3. Optical emission line fluxes from specific pseudo-slits or nebular regions.

Ion	I_{S_F} p-slit 1	I_{W_F} p-slit 1	I_F slit 1	$I_{S_{K1}}$ reg. 2	$I_{G_{K1}}$ reg. 2	$I_{S_{K4}}$ reg. 9	$I_{G_{K4}}$ reg. 9	$I_{S_{R1}}$ reg. 5	$I_{G_{R1}}$ reg. 5	$I_{S_{Neb}}$ p-slit 10	$I_{G_{Neb}}$ slit 10
He II 4686 Å	-	-	-	-	0.99	-	1.21	-	25.6	-	15.6
H I 4861 Å	100	100	100	100	100	100	100	100	100	100	100
[O III] 4959 Å	385	388	388	395	428	429	454	380	405	390	421
[N I] 5199 Å	0.048	-	0.089	4.11	6.06	4.10	2.82	0.005	-	0.143	0.11
He II 5412 Å	1.32	1.1	1.16	0.008	-	0.003	-	1.94	1.48	1.19	1.12
[Cl III] 5517 Å	0.435	0.5	0.454	0.860	-	0.932	1.03	0.377	0.46	0.566	0.58
[Cl III] 5538 Å	0.539	0.6	0.546	0.796	-	0.797	0.96	0.476	0.57	0.674	0.68
[N II] 5755 Å	0.336	-	0.395	5.21	6.95	5.38	4.19	0.187	0.15	0.530	0.5
He I 5876 Å	14.6	-	14.4	16.4	20.3	16.2	16.2	13.8	15.0	14.8	15.7
[O I] 6300 Å	0.355	0.4	0.553	25.2	31.0	21.7	14.8	0.013	-	1.01	1.06
[S III] 6312 Å	1.39	1.4	1.39	3.07	4.29	3.39	3.59	1.19	1.41	1.73	1.86
H I 6563 Å	288	-	266	290	394	290	224	291	312	291	313
[N II] 6584 Å	14.3	14.7	15.6	324	397	330	217	5.05	7.93	26.5	30.2
He I 6678 Å	3.88	4.0	3.68	4.4	8.41	4.40	3.57	3.71	4.35	3.93	4.46
[S II] 6717 Å	1.28	1.4	1.38	31.4	41.4	36.8	26.1	0.458	0.54	2.50	2.63
[S II] 6731 Å	2.18	2.3	2.28	43.8	57.4	45.3	32.0	0.818	0.95	4.12	4.34
[Ar III] 7136 Å	15.7	-	14.9	27.4	-	29.2	-	14.5	-	17.5	-
[O II] 7320 Å	1.36	1.3	1.19	8.56	-	7.45	-	1.09	-	1.63	-
[O II] 7330 Å	1.17	1.1	1.11	7.19	-	6.36	-	0.943	-	1.38	-
[S III] 9069 Å	24.5	25.2	23.2	48.7	-	51.3	-	19.7	-	29.9	-
F(H β)(10 ⁻¹³)	199	-	-	1.21	1.05	0.78	1.28	22.6	30.7	158	188
c(H β)	0.177	-	0.174	0.158	0.16	0.16	0.16	0.165	0.16	0.165	0.16
Te[N II]	11724	-	10780	10191	11000	10309	11700	14735	10400	10989	10300
Te[S III]	9272	-	11500	9677	9600 ^b	9877	10400 ^b	9453	10000 ^b	9293	10100 ^b
Ne[S II]	3661	-	4100	1628	2000	1059	1300	4959	5500	3100	4000
Ne[Cl III]	5150	-	3600	1862	-	1249	1900	5475	5200	4557	1300
He ⁺ (5876)/H ⁺	0.093	-	0.103	0.11	0.10	0.11	0.096	0.074	0.095	0.096	0.098
He ⁺ (6678)/H ⁺	0.088	-	0.095	0.11	-	0.11	-	0.070	-	0.091	-
He ⁺⁺ (5412)/H ⁺	0.014	-	0.013 ^c	0.00008	-	0.00003	-	0.021	0.012 ^c	0.013	0.013 ^c
He/H	0.109	-	0.112	0.11	0.10	0.11	0.096	0.094	0.108	0.106	0.111
N ⁰ /H ⁺ (-7)	1.13	-	0.84	96.8	87.0	75.3	27.0	0.07	-	3.72	2.7
N ⁺ /H ⁺ (-6)	2.02	-	2.73	62.7	50.0	61.6	23.8	43.7	1.10	4.31	4.45
ICF(N) ^a	67.3/-	-	-	3.94/7.06	7.8	4.13/8.44	10.6	264/-	64.7	38.0/-	38.2
N/H ^a (-5)	13.6/-	-	7.01 ^d	24.7/44.3	38.0	25.5/52.1	25.0	11.6/-	7.0	16.5/-	17.0
O ⁰ /H ⁺ (-6)	0.39	-	0.84	44.4	45.0	36.6	18.0	0.07	0.5	1.36	1.71
O ⁺ /H ⁺ (-5)	0.87	-	1.99	15.6	7.5	14.9	4.2	21.5	0.7	1.53	1.2
O ⁺⁺ /H ⁺ (-4)	5.20	-	3.23	4.59	5.12	4.65	4.1	4.80	4.12	5.22	4.21
ICF(O) ^a	1.10/1.09	-	1.086	1.0/1.0	1.0	1.09/1.08	1.00	1.18/1.16	1.08	1.09/1.08	1.08
O/H ^a (-4)	5.83/5.75	-	3.6	6.16/6.16	5.8	5.86/5.79	4.5	5.70/5.59	4.5	5.86/5.79	4.71
S ⁺ /H ⁺ (-7)	1.06	-	1.19	24.0	22.1	23.2	10.1	0.28	0.44	2.17	2.09
S ⁺⁺ /H ⁺ (-6)	4.18	-	2.26	7.74	7.45	7.86	4.8	3.24	2.1	5.11	3.3
ICF(S) ^a	2.83/-	-	?	1.20/1.09	1.43	1.13/1.11	1.57	4.46/-	2.79	2.36/-	2.35
S/H ^a (-6)	12.2/-	-	13.0	12.1/11.1	13.9	12.3/11.3	9.3	14.6/-	6.1	12.5/-	8.3
Cl ⁺⁺ /H ⁺ (-8)	8.65	-	5.51	11.8	-	11.3	-	7.15	-	10.8	-
ICF(Cl) ^a	-2.92 ^e	-	?	-/-	-	-/-	-	-3.90 ^e	-	-2.37	-
Cl/H ^a (-7)	-2.36 ^e	-	1.93	-/-	-	-/-	-	-2.79 ^e	-	-2.55	-
Ar ⁺⁺ /H ⁺ (-6)	1.56	-	1.03	2.43	-	2.46	-	1.36	-	1.71	-
ICF(Ar) ^a	1.87/-	-	?	1.87/1.19	-	1.87/1.21	-	1.87/-	-	1.87/-	-
Ar/H ^a (-6)	2.92/-	-	2.57	4.55/2.91	-	4.61/2.98	-	2.54/-	-	3.20/-	-

I is the intensity of the lines in the scale where H β = 100. The indices S, W, F, and G point out the results obtained with SATELLITE or from previous studies: (Walsh et al. 2018), (Fang & Liu 2011) and (Gonçalves et al. 2003). The indices K1, K4, R and Neb correspond to the sub-structures and total nebula based on Gonçalves et al. (2003). ^a Elemental abundances are provided using the ICFs from Kingsburgh & Barlow (1994) (left) and Delgado-Inglauda et al. (2014) (right), ^b These values correspond to the Te[O III] values, ^c He II 4686Å line is used for the computation of the ionic abundance, ^d Recombination and collisionally excited lines from UV, optical and IR were used to determine the abundance, ^e SATELLITE does not calculate/provide the total abundance and ICF of Cl because it lies outside the range of validity. “?” = unknown value.

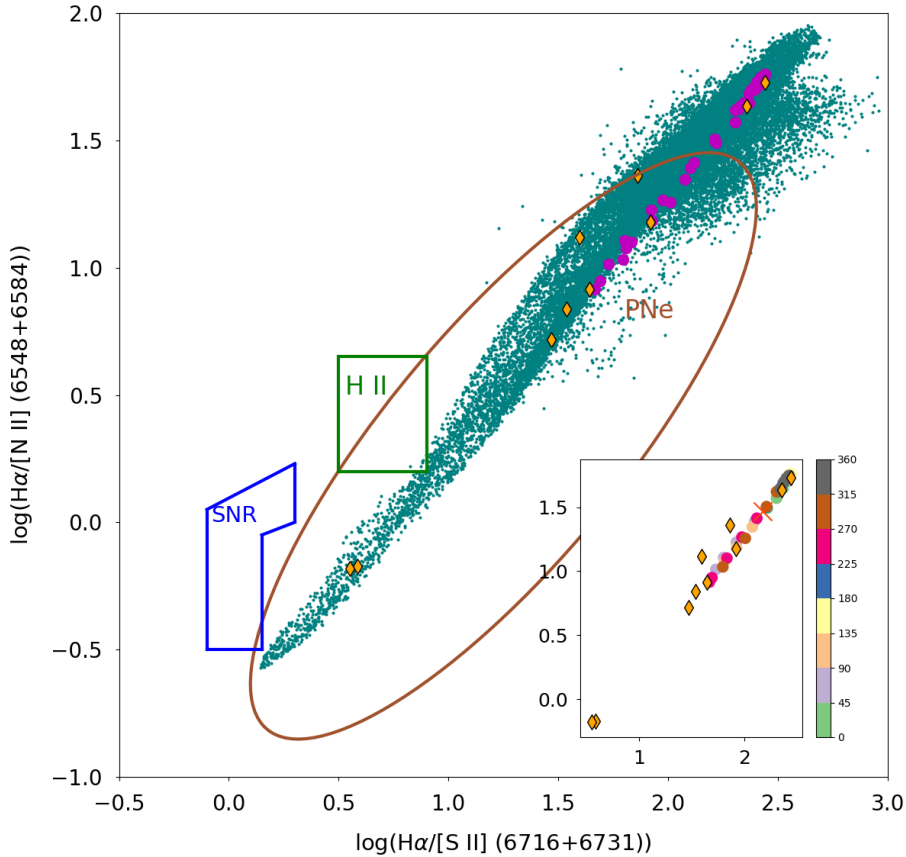


Figure 11. $\log(H\alpha/[S\ II] \ 6716+6731)$ versus $\log(H\alpha/[N\ II] \ 6548+6584)$ diagnostic diagram of NGC 7009 as a representative example. Cyan dots correspond to the values of individual spaxels, pink circles and yellow diamonds show the values obtained from the pseudo-slits of the *rotational analysis* module with position angles from 0 to 360 degrees with 10 degrees step and the values from the 10 pseudo-slits in the *specific slits analysis* module, respectively. The inset plot illustrate the variation of the line ratios with position angles of the pseudo-slits. The regimes of the PNe, H II regions and supernova remnants are also drawn (Sabbadin et al. 1977; Riesgo & López 2006; Frew & Parker 2010; Sabin et al. 2013).

Sabin et al. 2013) whereas pseudo-slits from the *rotation analysis* and *specific slit analysis* modules do not display such low ratios. Interestingly, two pseudo-slits from the *specific slit analysis* module (pseudo-slits 2 and 9) have the lowest values ($\log(H\alpha/[S\ II]) \sim -0.5$ and $\log(H\alpha/[N\ II]) \sim -0.5$) and correspond to the extracted windows from the two LISs/knots K1 and K4. Our mean values of the $H\alpha/[S\ II]$ and $H\alpha/[N\ II]$ ratios for the K1 and K4 knots agree with the results from HST imaging Phillips et al. (2010) but we do not observe the same distribution for individual spaxels. In particular, HST data display $H\alpha/[S\ II]$ and $H\alpha/[N\ II]$ ratio values well distributed in the SNRs regime (see fig. 19 in Phillips et al. 2010) while the distribution of the individual MUSE spaxels is within the PNe regime. Hence, we argue that any contribution of shocks in the knots of NGC 7009 is indistinguishable.

It is evident that line ratios can vary significantly from one sub-structure to another. The main nebula of NGC 7009 is certainly UV dominated and all its physical properties as well as emission line ratios can be explained from the strong UV radiation field of its central star. However, there are sub-structures like K1 to K4 LISs that diverge from the main bulk (Fig. 11). To explain the large divergence of line ratios in different sub-structures in the nebula with

comparable physical parameters (Table 3), a high density gas should be considered in these sub-structures. The detection of H_2 emission from the LISs in NGC 7009 (Akras et al. 2020b) supports the presence of a high density gas. The enhancement of low-ionisation emission such as $[N\ II]$, $[O\ I]$ emission lines in conjunction with the H_2 emission implies the presence of mini-photodissociation regions (PDRs). Furthermore, the detection of an emission at 8727\AA very likely associated with the red- $[C\ I]$ line (Akras et al. 2021 in preparation), found in PDRs (Burton et al. 1992, e.g.) and PNe (Liu et al. 1995), further supports the scenario that the enhanced emission from the low-ionization species found in the LISs of NGC 7009 originate from the partially ionized gas of mini-PDRs rather than shock-heated gas.

SATELLITE also calculates the mean value, standard deviation and the percentiles of 5%, 25% (Q1), 50% (median), 75% (Q3), 95% for each parameter with 2D maps constructed, such as $c(H\beta)$, T_e , and N_e , ionic abundances and line ratios (Table 4) (see also, Monreal-Ibero & Walsh 2020).

Table 4. Statistical results of NGC 7009 MUSE datacube.

Parameter	Num. of pix.	5% value	25% value	50%	75% value	95% value	mean	SD
c(H β)	40841	0.011	0.053	0.108	0.145	0.193	0.105	0.065
Te(NII6548_84)_Ne(SII6716_31)	19554	10000	10900	12100	13500	18700	13000	3200
Ne(SII6716_31)_Te(NII6548_84)	19554	828	1550	2490	3660	6870	3040	2090
Te(SIII6312_9069)_Ne(SII6716_31)	26658	8770	9000	9220	9480	10800	9420	749
Ne(SII6716_31)_Te(SIII6312_9069)	26658	615	1160	1930	3030	6100	2570	2300
Te(SIII6312_9069)_Ne(CIII5517_38)	17305	8780	8950	9130	9270	9700	9170	301
Ne(CIII5517_38)_Te(SIII6312_9069)	17305	1010	2060	3220	4610	7070	3610	2040
log(He I 5876/H α)	40017	-1.33	-1.27	-1.26	-1.25	-1.22	-1.26	0.04
log(He II 5412/H β)	14528	-3.05	-2.88	-2.53	-2.13	-1.64	-2.44	0.48
log(He I 5876/He II 5412)	14526	0.76	1.22	1.74	2.05	2.26	1.63	0.51
log([N II] 6584/H α)	40228	-1.87	-1.70	-1.55	-1.42	-0.69	-1.46	0.38
log((([N II] 6548,6584)/([O III] 4959,5007)))	40214	-2.52	-2.39	-2.25	-2.11	-1.35	-2.15	0.38
log([N I] 5200/H β)	5232	-3.22	-3.06	-2.64	-2.23	-1.10	-2.48	0.66
log((([S II] 6716,6731)/H α))	28808	-2.46	-2.25	-2.08	-1.90	-1.14	-1.98	0.42
log([S II] 6716/[S II] 6731)	28808	-0.29	-0.23	-0.17	-0.11	0.0001	-0.16	0.09
log((([S II] 6716,6731)/([S III] 6312,9069)))	27687	-1.27	-1.06	-0.91	-0.82	-0.32	-0.88	0.30
log([O I] 6300/H α)	11752	-3.80	-3.71	-3.16	-2.62	-1.25	-2.95	0.83
log([O III] 5007/H β)	40734	1.05	1.07	1.12	1.20	1.28	1.14	0.08
log((([O II] 7320,7330)/([O III] 4959,5007)))	22637	-3.15	-3.06	-2.97	-2.86	-2.45	-2.91	0.24
log((([Cl III] 5517,5538)/H β))	18176	-2.10	-2.03	-1.97	-1.92	-1.80	-1.96	0.09
abundance (He I 5876Å)	17305	0.088	0.102	0.108	0.110	0.113	0.105	0.008
abundance (He I 6678Å)	17305	0.083	0.096	0.103	0.105	0.109	0.099	0.008
abundance (He II 5412Å)	14052	9.39e-04	1.39e-03	3.09e-03	8.16e-03	2.48e-02	7.21e-03	8.13e-03
abundance ([O I] 6300 Å)	8948	1.14e-07	1.47e-07	2.83e-07	7.71e-07	1.75e-05	4.32e-06	1.61e-05
abundance ([O II] 7320 Å)	17298	1.69e-05	2.40e-05	2.90e-05	3.30e-05	6.60e-05	3.49e-05	3.15e-05
abundance ([O II] 7330 Å)	17285	1.82e-05	2.59e-05	3.14e-05	3.56e-05	6.48e-05	3.72e-05	3.29e-05
abundance ([O III] 5007 Å)	17305	4.44e-04	5.32e-04	5.73e-04	6.01e-04	6.62e-04	5.67e-04	6.85e-05
abundance ([N I] 5199 Å)	3646	3.22e-07	4.10e-07	6.73e-07	1.52e-06	1.53e-05	3.05e-06	7.26e-06
abundance ([N II] 5755 Å)	16705	2.64e-06	3.29e-06	4.36e-06	5.96e-06	2.42e-05	8.37e-06	1.52e-05
abundance ([N II] 6584 Å)	17305	8.35e-07	1.34e-06	2.03e-06	3.21e-06	1.85e-05	5.69e-06	1.44e-05
abundance ([S II] 6717 Å)	17301	5.17e-08	8.23e-08	1.29e-07	2.15e-07	1.00e-06	3.18e-07	6.91e-07
abundance ([S II] 6731 Å)	17305	5.06e-08	7.97e-08	1.20e-07	2.00e-07	9.18e-07	2.93e-07	6.11e-07
abundance ([S III] 6312 Å)	17305	2.63e-06	3.35e-06	4.06e-06	5.00e-06	7.48e-06	4.49e-06	1.55e-06
abundance ([S III] 9069 Å)	17305	2.63e-06	3.35e-06	4.06e-06	5.00e-06	7.48e-06	4.49e-06	1.55e-06
abundance ([Cl III] 5517 Å)	17305	6.57e-08	8.47e-08	9.83e-08	1.10e-07	1.36e-07	9.98e-08	2.36e-08
abundance ([Cl III] 5538 Å)	17305	6.57e-08	8.47e-08	9.83e-08	1.10e-07	1.36e-07	9.98e-08	2.36e-08
abundance ([Ar III] 7136 Å)	17305	1.16e-06	1.40e-06	1.60e-06	1.79e-06	2.25e-06	1.65e-06	3.37e-07

50% percentiles corresponds to the median.

4 THE CASE STUDY OF NGC 7009 WITH DEEPER MUSE DATA

Besides the SV MUSE data, deeper observations were also obtained in visitor mode on 07 July 2016 (097.D-0241(A), PI: R. L. M. Corradi; hereafter Cor MUSE data) using the extended mode. Short and long observations were obtained with exposure times of 30 and 150 sec, respectively. For the long exposure observations ten frames were obtained at different position angles resulting in total integrated times of 1500 sec. The DIMM seeing during the observations varied from 0.8 to 1.2 arcsec and the airmass changed from 1.126 to 1.357. Unfortunately, these observations were not carried out under photometric conditions due to the presence of thin cirrus. For consistency with the SV data, we found that the short and long exposure line maps of the Cor MUSE datacubes should be multiplied by 0.46 ± 0.05 and 2.4 ± 0.1 , respectively. This introduces an extra uncertainty on the analysis but it is valuable to verify the performance of SATELLITE using the flux maps from a second datacube and an independent reduction and emission line fitting.

Line intensities, physical parameters (c(H β), T_e , N_e) and abun-

dances computed from the pseudo-slits 1, 10 (Fig. 3) and the entire nebula (2310 square arcseconds) obtained with the SATELLITE code from the SV and Cor MUSE data are listed in Table 5. The comparison of the line intensities between the two datacubes is displayed in Fig. 12. A reasonable matching is also found for all the nebular parameters. Only the extinction coefficient exhibits an unexpected mismatch of the order or 25 percent, due to the non-photometric night. Thus, within the involved uncertainties, the results validate the *specific slit analysis* module of the SATELLITE code for the spectroscopic analysis of specific regions or sub-structures in PNe such as knots.

The results from the *rotation analysis* and *radial analysis* modules are also consistent between the two datasets. All the nebula parameters show the same behaviour with the PA of the pseudo-slits and similar absolute values (not presented here). The high T_e [N II] values at the PAs of 0, 150 and 320 degrees are found again with the Cor MUSE data. The radial profiles of the nebular parameter are also comparable. T_e [N II] is higher at the central region of the nebula and

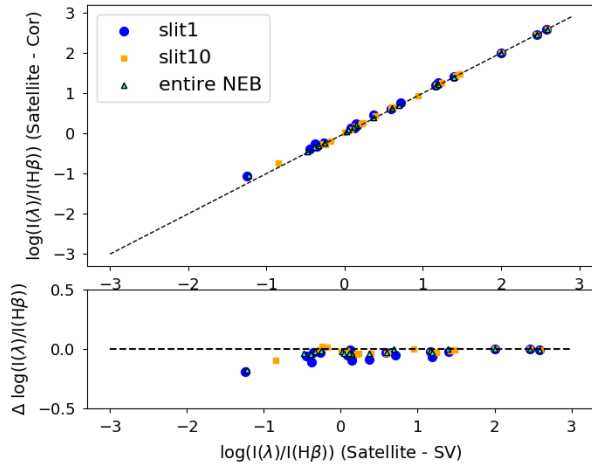


Figure 12. Comparison of the line ratios relative to $H\beta=100$ obtained from the pseudo-slits 1, 10 and the entire nebula of NGC 7009 from two MUSE datacubes using *SATELLITE*: science verification MUSE data (SV), (Walsh et al. 2018) and the Cor MUSE data (097.D-0241(A), PI: R. L. M. Corradi).

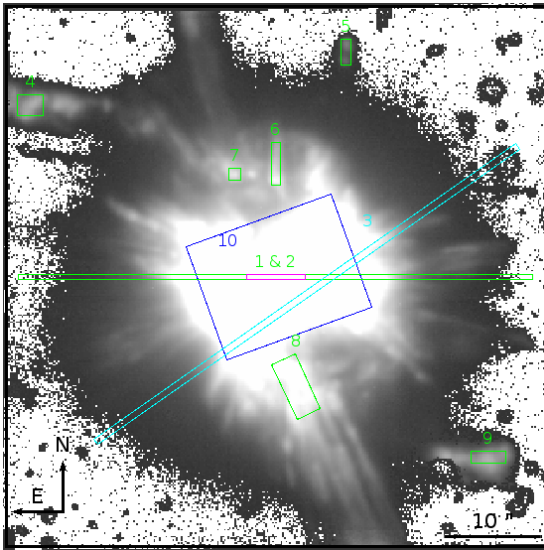


Figure 13. 10 slits/regions selected for the spectroscopic analysis of specific slits with *SATELLITE* are overlaid on the $[N\text{ II}]\ \lambda 6584$ line map of NGC 6778. North is up east to the left.

decreases for larger distance while $T_e[S\text{ III}]$ is nearly constant. As for the electron density, very small differences are found.

For the 2D analysis module, the results of the statistical analysis of the Cor MUSE maps, for instance the mean values, standard deviations and the 5%, 25% (Q1), 50% (median), 75% (Q3) and 95% percentiles provide an overall consistency between the two set datacubes.

5 THE CASE STUDY OF NGC 6778 WITH COR MUSE DATA

In this section, we present the spectroscopic analysis of the planetary nebula NGC 6778 employing the *SATELLITE* code and MUSE data

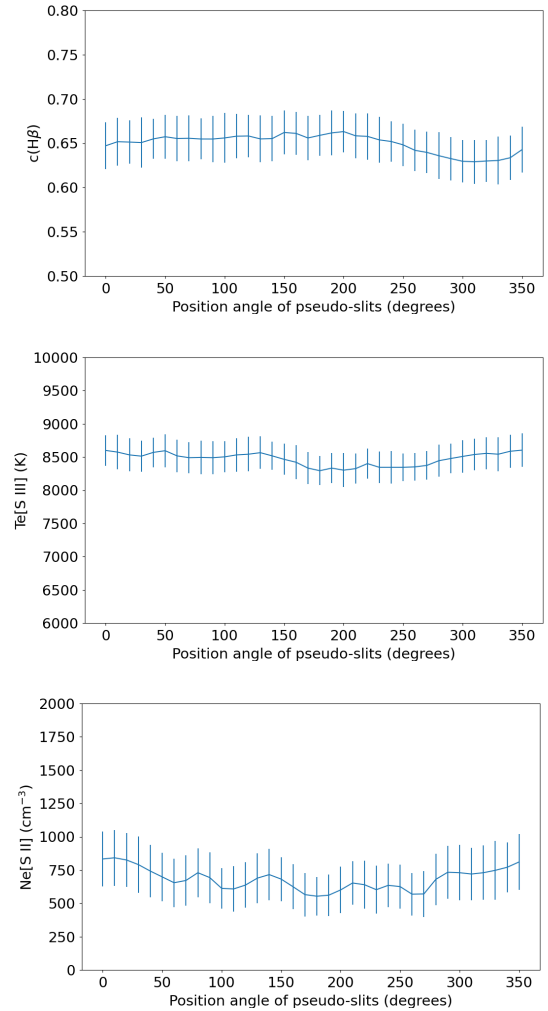


Figure 14. $c(H\beta)$, $T_e[S\text{ III}]$ and $N_e[S\text{ II}]$ as functions of the pseudo-slit position angles for NGC 6778

(097.D-0241(A), PI: R. L. M. Corradi). NGC 6778 has a complex morphology with a bright waist, a number of low-ionization knots and two pairs of collimated jets (Guerrero & Miranda 2012). What makes this nebula an intriguing object is its central star which has been found to be a close binary system with a period of ~ 0.15 days (Miszalski et al. 2011). Binary systems in PNe have been linked with a high abundance discrepancy factor and NGC 6778 is one of them ($adf=20$, Jones et al. 2016).

Recent data from OSIRIS Blue Tunable Filter (GTC) and VIMOS IFU (VLT) have revealed a significant difference in the spatial distribution between the $O\text{ II}\ 4649+50\text{Å}$ optical recombination lines (ORLs) and the collisionally excited $[O\text{ III}]\ \lambda 5007$ line (García-Rojas et al. 2016). Interestingly, the auroral $[O\text{ III}]\ \lambda 4363$ line displays the same spatial distribution as the $O\text{ II}$ recombination line resulting in questionable T_e (Gómez-Llanos et al. 2020). These results make NGC 6778 an ideal target for a 2D imaging spectroscopic analysis with deep MUSE data. A full presentation of the data and spatial analysis of the complete MUSE data set of NGC 6778, including $C\text{ II}$, $O\text{ II}$ and $N\text{ II}$ ORLs has been presented in García-Rojas et al. (2022). In this work with *SATELLITE*, we focus on the spectroscopic analysis of the nebula using the bright collisionally excited lines (CELs) and H/He recombination lines.

Table 5. Comparison between optical emission line fluxes and derived quantities from specific slits between SV and Cor MUSE data of NGC 7009.

Ion	I_{S_F} (SV) p-slit 1	I_{S_F} (Cor) p-slit 1	$I_{S_{Neb}}$ (SV) p-slit 10	$I_{S_{Neb}}$ (Cor) p-slit 10	$I_{S_{entire}}$ (SV) 2310 arcsec ²	$I_{S_{entire}}$ (Cor) 2310 arcsec ²
He II 4686 Å	-	17.5	-	16.4	-	14.3
H I 4861 Å	100	100	100	100	100	100
[O III] 4959 Å	385	391	390	396	388	395
[N I] 5199 Å	0.048	0.087	0.143	0.177	0.058	0.091
He II 5412 Å	1.32	1.35	1.20	1.24	1.04	1.10
[Cl III] 5517 Å	0.435	0.468	0.566	0.538	0.468	0.488
[Cl III] 5538 Å	0.539	0.578	0.674	0.645	0.554	0.575
[N II] 5755 Å	0.336	0.408	0.530	0.540	0.330	0.355
He I 5876 Å	14.6	15.4	14.8	15.6	14.9	15.7
[O I] 6300 Å	0.355	0.544	1.01	1.05	0.411	0.450
[S III] 6312 Å	1.39	1.60	1.73	1.86	1.39	1.50
[N II] 6548 Å	4.88	5.82	8.85	8.82	4.89	4.88
H I 6563 Å	288	289	291	289	288	289
[N II] 6584 Å	14.3	18.1	26.5	27.3	14.6	15.2
He I 6678 Å	3.88	4.12	3.93	4.20	3.98	4.24
[S II] 6717 Å	1.28	1.71	2.50	2.70	1.39	1.54
[S II] 6731 Å	2.18	2.88	4.12	4.41	2.32	2.53
[Ar III] 7136 Å	15.7	17.3	17.5	18.6	15.5	16.5
[O II] 7320 Å	1.36	1.58	1.63	1.78	1.29	1.41
[O II] 7330 Å	1.17	1.35	1.38	1.51	1.11	1.21
[S III] 9069 Å	24.5	26.3	29.9	30.3	24.8	24.9
<hr/>						
F(H β)(10 ⁻¹³)	199	208	158	159	1458	1469
c(H β)	0.170	0.221	0.165	0.211	0.166	0.218
Te[N II]	11724	11578	10989	10980	11547	11822
Te[S III]	9272	9516	9293	9566	9219	9498
Ne[S II]	3661	3493	3100	2999	3333	3167
Ne[Cl III]	5150	5127	4577	4776	4648	4435
<hr/>						
He ⁺ (5876)/H ⁺	0.093	0.098	0.096	0.102	0.096	0.10
He ⁺ (6678)/H ⁺	0.088	0.094	0.091	0.098	0.091	0.096
He ⁺⁺ (5412)/H ⁺	0.014	0.014 ^b	0.013	0.013 ^b	0.011	0.017 ^b
He/H	0.109	0.111	0.106	0.113	0.105	0.107
N ⁰ /H ⁺ (-7)	1.13	2.05	3.72	4.50	1.34	1.88
N ⁺ /H ⁺ (-6)	2.02	2.57	4.31	4.41	2.12	2.06
ICF(N) ^a	67.3/-	40.7/-	38.0/-	31.4/-	64.1/-	63.1/-
N/H ^a (-5)	13.6/-	12.9/-	16.5/-	13.9/-	13.7/-	13.8/-
O ⁺ /H ⁺ (-5)	0.87	1.09	1.53	1.72	0.92	0.95
O ⁺⁺ /H ⁺ (-4)	5.20	4.82	5.22	4.79	5.35	4.90
ICF(O) ^a	1.10/1.09	1.09/1.08	1.09/1.08	1.09/1.07	1.08/1.07	1.08/1.07
O/H ^a (-4)	5.83/5.75	5.41/5.34	5.86/5.79	5.40/5.33	5.87/5.81	5.36/5.30
S ⁺ /H ⁺ (-7)	1.06	1.41	2.17	2.32	1.13	1.15
S ⁺⁺ /H ⁺ (-6)	4.18	4.27	5.11	4.86	4.30	4.07
ICF(S) ^a	2.83/-	2.56/-	2.36/-	2.21/-	2.78/-	2.77/-
S/H ^a (-6)	12.2/-	11.3/-	12.5/-	11.3/-	12.3/-	11.6/-
Cl ⁺⁺ /H ⁺ (-8)	8.65	8.55	10.8	9.41	9.10	8.60
ICF(Cl) ^a	-/2.92 ^c	-/2.53	-/2.37	-/2.26	-/2.65	-/2.65
Cl/H ^a (-7)	-/2.36 ^c	-/2.17	-/2.55	-/2.13	-/2.42	-/2.23
Ar ⁺⁺ /H ⁺ (-6)	1.56	1.61	1.71	1.71	1.57	1.55
ICF(Ar) ^a	1.87/-	1.87/-	1.87/-	1.87/-	1.87/-	1.87/-
Ar/H ^a (-6)	2.92/-	3.01/-	3.20/-	3.20/-	2.93/-	2.89/-

^a Elemental abundances are provided using the ICFs from [Kingsburgh & Barlow \(1994\)](#) (left) and [Delgado-Inglada et al. \(2014\)](#) (right).

^b He II 4686Å line is used for the computation of the ionic abundance.

^c SATELLITE does not calculate/provide the total abundance and ICF of Cl because the criteria are not satisfied.

Fig. 13 illustrates the 10 pseudo-slits/regions selected for the spectroscopic exploration. The magenta slit (number 1) corresponds to the slit position from [Dufour et al. \(2015\)⁶](#). The green pseudo-slit 2

has the same width as the pseudo-slit 1, but it is 60 arcsec longer, in

wide. Moreover, [Dufour et al. \(2015\)](#) excluded a small region from -0.36 to 0.72 arcsec to avoid contamination from the central star and the spectrum is the result of the sum of two extracted windows (-3.24:-0.36 and 0.72:3.6).

⁶ Our pseudo-slit is 0.6 arcsec (3 pixel) wide while the real one is 0.5 arcsec

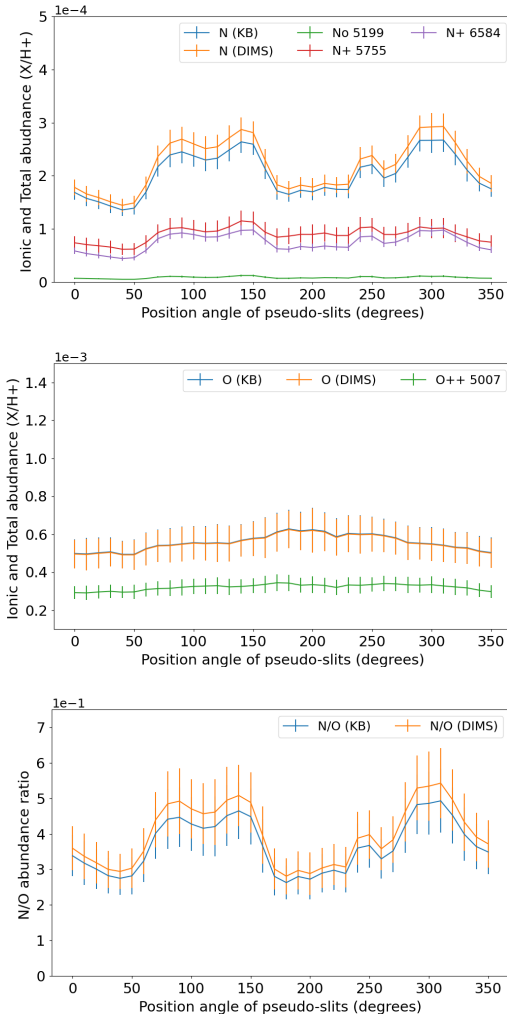


Figure 15. Ionic and total N (upper panel) and O (middle panel) abundances of NGC 6778 as well as a N/O ratio (lower panel) as a function of the pseudo-slit position angles. The total abundances is computed using the ICFs schemes from [Kingsburgh & Barlow \(1994\)](#) and [Delgado-Inglada et al. \(2014\)](#).

order to cover the nebula from one side to the other and compare the results with those from the pseudo-slit 1 centred only on the inner zone. The cyan pseudo-slit 3 corresponds to the slit of [Jones et al. \(2016\)](#)⁷ (PA=-55 degrees). Pseudo-slits 4 to 9 (green colour) cover a number of LISs distributed throughout the nebula. Finally, pseudo-slit 10 (blue colour) covers the whole central region of NGC 6778.

In Table 6, we present the interstellar extinction corrected line intensities for the pseudo-slits as well as the integrated spectrum for an area of 1602 square arcsec. The spectra from the pseudo-slits 1 and 3 are compared with the observations in [Dufour et al. \(2015\)](#) and [Jones et al. \(2016\)](#), respectively, and a very good agreement is found for the majority of the lines and physical parameters ($c(H\beta)$,

⁷ SATELLITE calculates the spectra from the entire pseudo-slit (length=6.84 arcsec).

⁷ The SATELLITE pseudo-slit and the one from [Jones et al. \(2016\)](#) do not correspond to the exact same regions. In particular, our pseudo-slit is slightly wider than the real one. It has a width of 0.8 arcsec (4 pixel) while the real one is 0.7 arcsec wide. Moreover, there was an offset between the red and blue exposures in [Jones et al. \(2016\)](#), which we do not take into account.

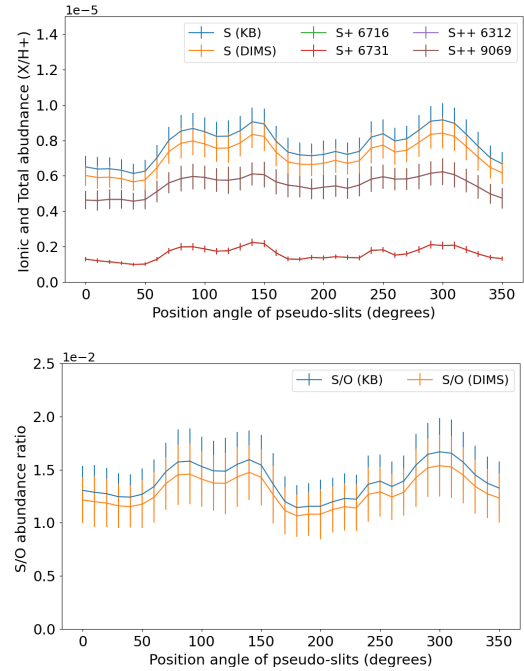


Figure 16. Ionic and total S (upper panel) abundances and S/O ratio (lower panel) of NGC 6778 as a function of the pseudo-slit position angles. The total abundances is computed using the ICFs schemes from [Kingsburgh & Barlow \(1994\)](#) and [Delgado-Inglada et al. \(2014\)](#). The ionic abundances derived from [S II] $\lambda 6716$ and $\lambda 6731$, and [S III] $\lambda 6312$ and $\lambda 9069$ emission lines are very similar which makes one overlays the other.

T_e and N_e). The integrated $F(H\beta)$ flux of the whole nebula is being $5.72 \times 10^{-12} \text{ erg s}^{-1} \text{ cm}^{-2}$, in reasonable agreement with the value of $6.92 \times 10^{-12} \text{ erg s}^{-1} \text{ cm}^{-2}$ found by [Acker et al. \(1992\)](#).

The extinction coefficient is found to be 0.65 with a standard deviation of 0.02 between the values reported by [Dufour et al. \(2015\)](#) and [Jones et al. \(2016\)](#). $T_e[S \text{ III}]$ and $N_e[S \text{ II}]$ measured for the pseudo-slits vary from 8300 to 8600 K and from 550 to 850 cm^{-3} , respectively, in agreement with the literature.

Chemical abundances are provided only by [Jones et al. \(2016\)](#) and can be compared with those obtained for the pseudo-slit 3. Despite the agreement in the line intensities and T_e/N_e , a significant difference in the chemical abundances is found. In particular, we find slightly higher He, twice higher O and S, half N and comparable or half Ar abundances depending on the ICF. This discrepancy in abundances is associated to a combination of the different extinction, physical conditions, atomic data sets and ICFs adopted. A more detailed analysis of such differences has been presented in [García-Rojas et al. \(2022\)](#). All chemical abundances derived from the pseudo-slits and the central region (Table 6) show small variations, within their uncertainties.

The next step is the spectroscopic analysis of the pseudo-slit spectra as a function of the position angles (PA). $c(H\beta)$, $T_e[S \text{ III}]$ and $N_e[S \text{ II}]$ show no variability with PAs and their values are approximately 0.66, 8500 K and 680 cm^{-3} , with standard deviations of 0.01, 100 K and 80 cm^{-3} , respectively (Fig. 14).

Regarding the chemical abundances, He and O appear unchanged with PAs, while N and S show an enrichment at $80 < \text{PA} < 150$ and $260 < \text{PA} < 340$ degrees (see Figs 15 and 16). The N/O and S/O abundances ratios also appear to vary with PAs but they can be considered constant at ~ 0.35 and ~ 0.014 within the errors, respectively. This

Table 6. Optical emission line intensities from the specific slit task of NGC 6778

Ion	I_{S_D} p-slit 1	I_D slit 1	I_{S_D} ext [†] p-slit 2	I_{S_J} p-slit 3	I_J slit 3	I_S p-slit 4	I_S p-slit 6	I_S p-slit 8	I_S p-slit 9	I_S p-slit 10	$I_S^{\dagger\dagger}$ 1602 arc ²
He II 4686 Å	17.4	19.8	8.26	4.07	6.50	13.4	1.66	0.624	11.4	5.69	5.10
H I 4861 Å	100	100	100	100	100	100	100	100	100	100	100
[O III] 4959 Å	171	171	171	169	171.11	99.5	119	141	92.3	171	167
[N II] 5199 Å	2.12	-	2.69	2.46	-	15.8	1.60	3.50	13.5	2.99	3.15
[Cl III] 5517 Å	0.548	-	0.646	0.652	-	5.84	0.610	0.672	6.02	0.633	0.715
[Cl III] 5538 Å	0.465	-	0.556	0.553	-	6.08	0.489	0.557	5.65	0.544	0.615
[N II] 5755 Å	2.58	-	2.76	2.40	-	11.2	1.34	2.39	9.98	2.91	2.87
He I 5876 Å	23.0	26.1	23.2	23.4	22.12	27.0	23.7	23.3	25.2	23.3	23.4
[O I] 6300 Å	3.34	-	4.41	3.81	3.69	32.1	1.66	5.15	24.9	4.97	5.05
[S III] 6312 Å	1.09	-	1.19	1.11	1.05	4.34	0.695	0.905	2.64	1.21	1.20
H I 6563 Å	296	286	296	296	289.88	297	297	297	296	297	296
[N II] 6584 Å	195	153	257	229	226.65	879	142	302	981	282	279
He I 6678 Å	6.57	8.54	6.65	6.72	6.61	9.41	6.79	6.64	7.90	6.69	6.71
[S II] 6717 Å	14.3	12.9	19.3	17.1	16.92	59.7	12.1	24.78	64.3	20.8	21.1
[S II] 6731 Å	16.3	14.7	21.0	18.1	18.00	44.9	11.1	23.7	48.9	23.1	22.6
[Ar III] 7136 Å	14.6	11.0	16.8	16.4	-	19.6	13.2	17.1	20.2	17.4	17.3
[O II] 7320 Å	3.14	-	2.58	2.30	-	4.99	1.25	1.56	4.52	2.51	2.29
[O II] 7330 Å	2.54	-	2.08	1.88	-	8.39	1.13	1.26	4.99	2.04	1.20
[S III] 9069 Å	23.7	17.7	27.6	27.3	-	18.1	21.6	22.8	20.5	28.4	27.8
F(H β)(10 ⁻¹⁴)	10.7	3.09	27.6	26.6	-	0.05	0.79	5.77	0.04	465	572
c(H β)	0.65	0.74	0.65	0.65	0.46	0.69	0.65	0.65	0.60	0.65	0.64
Te[N II]	9524	10300 ^a	8830	8769	8850 ^b	9441	8472	7996	8704	8689	8697
Te[S III]	8578	-	8388	8219	8800 ^b	22454 ^c	7591	8139	13945 ^c	8329	8374
Ne[S II]	781	919	661	586	590	90	318	380	100	685	610
Ne[Cl III]	1179	-	1262	1156	-	3308	784	1014	2054	1249	1262
He ⁺ (5876)/H ⁺	0.161	-	0.161	0.163	0.154	-	0.163	0.163	-	0.162	0.163
He ⁺ (6678)/H ⁺	0.161	-	0.163	0.164	-	-	0.164	0.162	-	0.164	0.164
He ⁺⁺ (4686)/H ⁺	0.014	-	0.007	0.003	-	-	0.013	0.001	-	0.001	0.004
He/H	0.175	-	0.169	0.167	0.159	-	0.165	0.163	-	0.167	0.168
N ⁰ /H ⁺ (-6)	7.13	-	9.50	9.16	-	-	7.42	12.2	-	11.1	10.0
N ⁺ /H ⁺ (-5)	5.99	-	8.48	7.99	5.55	-	6.37	1.09	-	9.58	9.31
ICF(N)	2.51/2.54	-	2.56/2.79	2.52/2.94	?	-	2.21/2.76	2.62/3.71	-	2.56/2.90	2.57/2.93
N/H (-4)	1.51/1.52	-	2.17/2.36	2.01/2.35	4.04	-	1.41/1.76	2.88/4.06	-	2.45/2.77	2.39/2.73
O ⁰ /H ⁺ (-6)	12.0	-	17.4	16.0	-	-	11.1	22.9	-	20.1	20.2
O ⁺ /H ⁺ (-4)	2.24	-	2.26	2.33	0.56	-	2.98	1.95	-	2.29	2.18
O ⁺⁺ /H ⁺ (-4)	3.08	-	3.37	3.62	2.83	-	3.58	3.15	-	3.46	3.34
ICF(O)	1.06/1.05	-	1.03/1.02	1.01/1.01	?	-	1.00/1.00	1.00/1.00	-	1.02/1.02	1.02/1.01
O/H (-4)	5.63/5.58	-	5.78/5.76	6.14/6.12	3.39	-	6.60/6.59	5.11/5.11	-	5.86/5.84	5.58/5.57
S ⁺ /H ⁺ (-6)	1.33	-	1.84	1.67	1.44	-	1.34	2.29	-	2.06	1.98
S ⁺⁺ /H ⁺ (-6)	4.88	-	5.99	6.21	4.26	-	5.97	5.34	-	6.27	6.06
ICF(S)	1.09/1.02	-	1.09/1.01	1.09/1.01	?	-	1.06/1.0	1.09/1.01	-	1.09/1.0	1.09/1.00
S/H (-5)	0.68/0.63	-	0.85/0.78	0.86/0.78	0.34	-	0.78/0.71	0.84/0.76	-	0.91/0.83	0.88/0.80
Cl ⁺⁺ /H ⁺ (-7)	1.04	-	1.33	1.43	-	-	1.75	1.51	-	1.34	1.49
ICF(Cl)	-1.37	-	-1.34	-	?	-	-	-	-	-1.33	-1.33
Cl/H (-7)	-1.43	-	-1.79	-	-	-	-	-	-	-1.79	-1.97
Ar ⁺⁺ /H ⁺ (-6)	1.78	-	2.16	2.25	3.80	-	2.28	2.39	-	2.29	2.24
ICF(Ar)	1.87/1.11	-	1.87/1.10	1.87/1.09	?	-	1.87/1.05	1.87/1.09	-	1.87/1.09	1.87/1.09
Ar/H (-6)	3.32/1.98	-	4.05/2.36	4.20/2.44	4.68	-	4.26/2.39	4.47/2.61	-	4.28/2.51	4.19/2.45

I is the intensity of the lines. The indices S, D, and J point out the results obtained with SATELLITE or from previous studies: Dufour et al. (2015) and Jones et al. (2016), [†] Extended pseudo-slit, ^{††} Integrated from an area of 1602arc², ^a: Dufour et al. (2015) use this value as default and do not provide ionic and total abundances, ^b: T_e is derived from [S II] (row: T_e[N II]) and [O III] (row: T_e[S III]) lines, ^c: Very uncertain T_e values. Chemical abundances are not provided for this very faint pseudo-slits, “?”=unknown value

specific range of PAs, with enhanced N and S abundances, does not correspond to any particular knot or jet in NGC 6778, rather the equatorial waist of the nebula which is known to display a filamentary wisp structure bright in [N II] λ 6584 line (Guerrero & Miranda 2012).

In order to further investigate the issue just discussed, the radial analysis of NGC 6778 as a function of the distance from the central star is performed for a pseudo-slit at PA=288 degrees across the equatorial waist (Fig. 17). No variation in the c(H β) is found with the distance from the CS up to 15 arcsec. T_e is nearly constant (~8500 K)

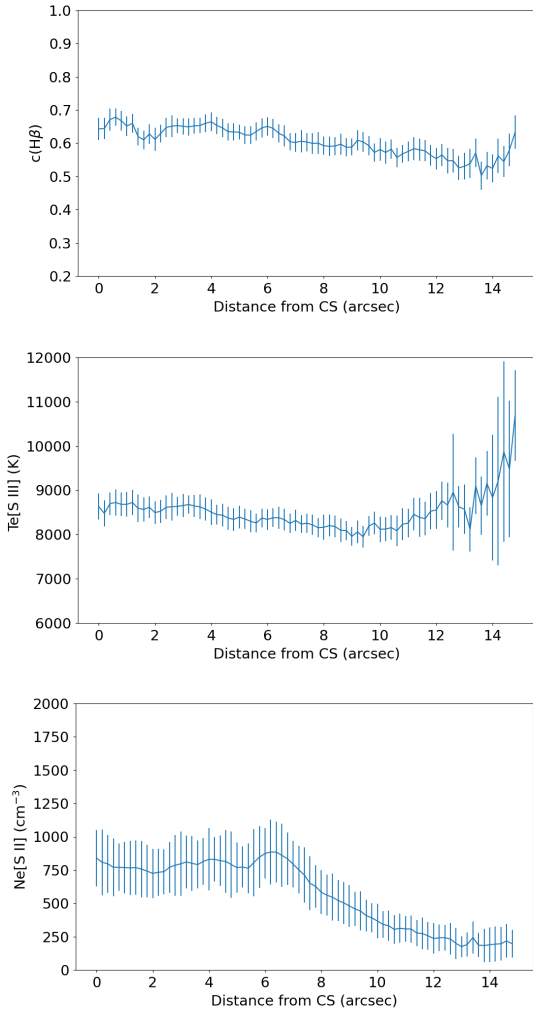


Figure 17. $c(\text{H}\beta)$, $T_e[\text{S III}]$ and $N_e[\text{S II}]$ of NGC 6778 as functions of the distance from the central star in arcsec obtained from a pseudo-slit at PA=288 degrees.

up to 10 arcsec and then starts increasing outwards. However, the high uncertainties do not allow to argue whether this increment of T_e for distances >10 arcsec is real, due to an extra heating mechanism. N_e is also constant ($\sim 800 \text{ cm}^{-3}$) for a distance up to ~ 7 arcsec and then smoothly decreases for larger distances down to $150/200 \text{ cm}^{-3}$.

The final part of the analysis of NGC 6778 is carried out through the 2-dimensional line maps which provide a better illustration of the spatial distribution for the nebular parameters. Fig. 18 displays the maps of $c(\text{H}\beta)$, $T_e[\text{S III}]$ and $N_e[\text{S II}]$. $c(\text{H}\beta)$ varies between 0.5 and 0.8. The values higher than 0.75 at the outskirts of the nebula are uncertain due to the low S/N ratio while the values lower than 0.55 found in the external parts of the disrupted equatorial component are likely real. Moreover, the 1D analysis returns a nearly constant value of 0.65 regardless of the PA of the pseudo-slit and it is in excellent agreement with the integrated value of 0.64 obtained with SATELLITE (Akras et al. 2022) and 0.66 from García-Rojas et al. (2022). A small spatial variation in $T_e[\text{S III}]$ is observed throughout the nebula. The central region is characterized by a higher temperature of $\sim 9000 \text{ K}$ while the rest of the nebula exhibits $T_e[\text{S III}] \sim 8500 \text{ K}$. On the other hand, $N_e[\text{S II}]$ map shows evident density clumps ($900 < N_e < 1200 \text{ cm}^{-3}$) distributed in a more tenuous central region with $N_e \sim 600 \text{ cm}^{-3}$.

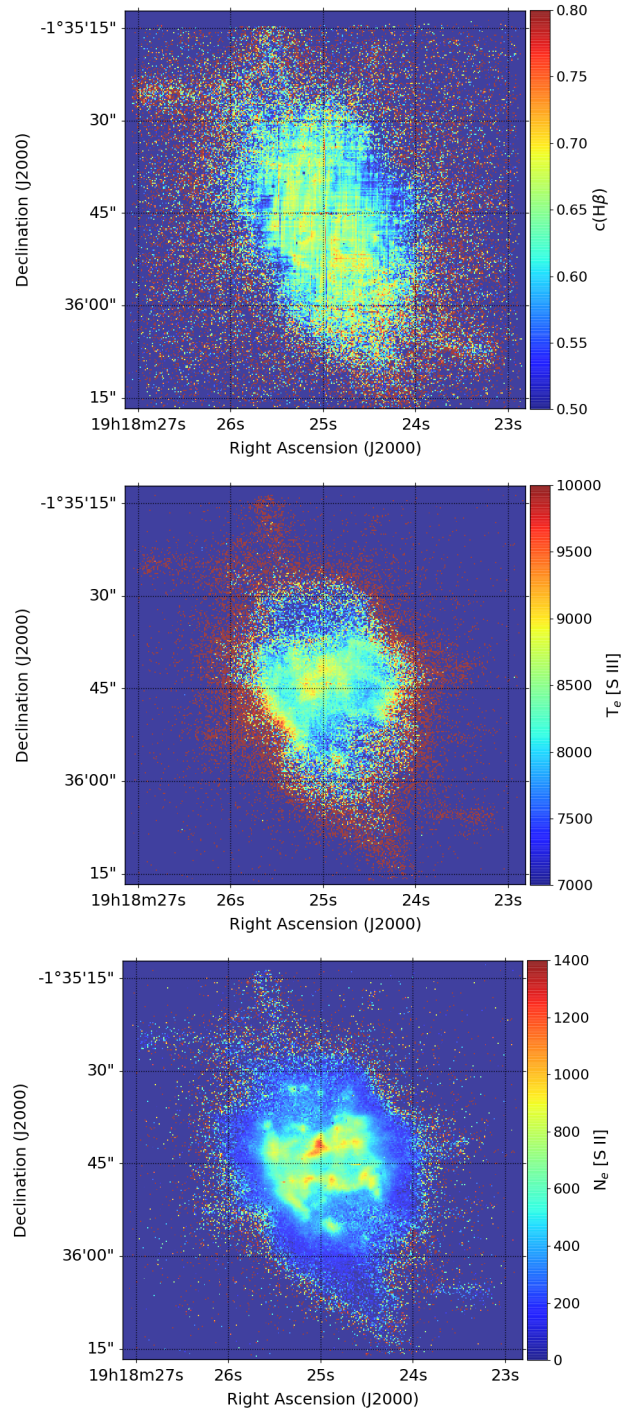


Figure 18. $c(\text{H}\beta)$ (upper), $T_e[\text{S III}]$ (middle), $N_e[\text{S II}]$ (lower) maps of NGC 6778.

As a representative example of a line ratio map provided by SATELLITE, in Fig. 19 we present the $\log([\text{O I}] 6300/\text{H}\alpha)$ map. The regions/knots 4,5 and 9 (see Fig. 13) are highlighted by this line ratio with value >-1 . The outer parts of the equatorial waist ($>8-9$ arcsec) also display higher $[\text{O I}] 6300/\text{H}\alpha$ ratio relative to the central part of the nebula (~ -2).

The emission line diagnostic diagram, extracted by SATELLITE, of the $\log([\text{O III}] 5007 \text{ \AA}/\text{H}\beta)$ versus $\log([\text{S II}] 6716+6731/\text{H}\alpha)$ is presented as a representative example of NGC 6778 (Fig. 20). The

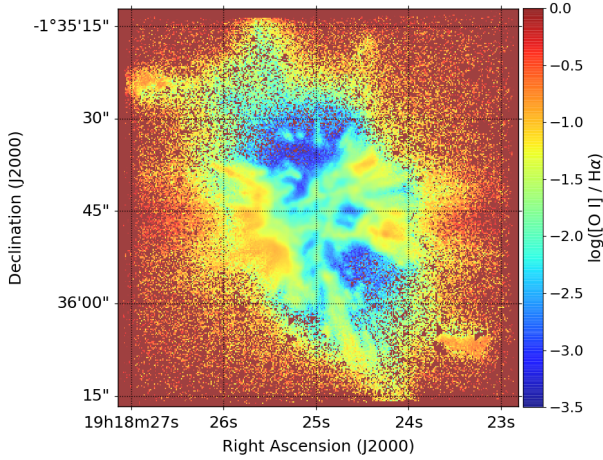


Figure 19. A representative example of a line ratio map of NGC 6778: $\log([\text{O I}]/\text{H}\alpha)$.

nebula is UV dominated as indicated by the line ratios from the bulk of spaxel (blue dots), the *rotation* (purple circles) and *specific slits analysis* (yellow diamonds) modules are well distributed in the loci of PNe and H II regions. It should be noted that two sub-structures of NGC 6778 display high $\log([\text{S II}] 6716+6731/\text{H}\alpha)$ and $\log([\text{N II}] 6548+6584/\text{H}\alpha)$ ratios, and they lie in a transition zone between the PNe and SNRs. These two sub-structures corresponds to the regions/pseudo-slit 4 and 9, two LISs at the end of the seemingly jet-like structures of NGC 6778 (see Fig. 13). Scrutinising all the diagnostic diagram provided by SATELLITE, we conclude that these two sub-structures are distinct from the main nebula lying at the outer edges of the spaxels' distribution. An additional shock-heated mechanism cannot be ruled out. Finally, Table 7 lists the mean values and percentiles of $c(\text{H}\beta)$, N_e , T_e and emission line ratios for the MUSE maps of NGC 6778.

6 DISCUSSION AND CONCLUSIONS

The transition from the traditional 1D long-slit spectroscopy to 2D imaging or integral field spectroscopy requires a proper interpretation of the results. To this end, a newly developed code written in PYTHON language – the Spectroscopic Analysis Tool for intEgral fieLd unIt daTacubEs (SATELLITE) – for the study of extended sources is presented. SATELLITE uses the 2D flux maps generated from the datacubes of any IFU to perform a full spectroscopic characterization of extended photoionized nebulae (PNe, H II regions, galaxies, etc.) combining 1D and 2D analysis.

In the current version of the SATELLITE code, four modules have been developed: (I) *rotation analysis*, (II) *radial analysis*, (III) *specific slits analysis* and (IV) *2D analysis* modules. The MUSE Science Verification data of NGC 7009 was used for the verification of the performance of the code.

A comparison of the resulting 2D maps of several nebular parameters obtained with SATELLITE and those from Walsh et al. (2018) show a discrepancy less than 5 per cent, except for the abundance of singly ionized oxygen (O^+/H^+) for which the difference is of ~ 20 percent due to the recombination contribution to the $[\text{O II}] \lambda\lambda 7320, 7330$ lines. In addition to the 2D maps, 1D spectroscopic analysis through 10 pseudo-slits resulted in a good agreement with previous long-slit spectroscopic studies. The evaluation of SATELLITE's outcomes

was carried out using two different MUSE datasets of NGC 7009, verifying the efficiency and consistency of the code.

SATELLITE was also applied to the MUSE data of NGC 6778. A satisfactory agreement was found for the emission line intensities and physical parameters between SATELLITE and long-slit studies in the literature.

The most noteworthy results from the spectroscopic analysis of the PNe studied in this work are:

- The good agreement between the pseudo-slit spectra and the observed ones from long-slit spectroscopy in the literature (1D analysis).
- The variation of the line flux (or line ratios) as a function of the distance from the central star of NGC 7009 and the clear offset between the low and moderate/high ionization emission line (1D radial analysis).
- The perceptible augmentation of $c(\text{H}\beta)$ and T_e in the LISs of NGC 7009 but not of NGC 6778 (1D and 2D analysis).
- The non-negligible spatial variation in $c(\text{H}\beta)$, N_e , T_e and emission line ratios throughout both nebulae (2D analysis).
- The clear dispersion of sub-structures/features in the emission line diagnostic diagrams associated either with their ionization structure or the excitation mechanism (1D and 2D analysis).
- A spaxel-by-spaxel analysis of IFUs datacubes cannot be applied to emission line ratio diagnostic diagrams for distinguishing photo-ionized and shock-heated regions in resolved PNe (1D and 2D analysis).
- NGC 6778 shows considerable ionic abundance variations in N and S with the PAs of the pseudo-slits probably due to the ICFs, being enhanced in the direction of the equatorial waist (1D and 2D analysis). However, this variation is lessened in the abundances ratios.
- A discrepancy of ~ 0.3 dex in the chemical abundances of NGC 6778 is found between the pseudo-slit 3 and the spectrum from Jones et al. (2016) is probably associated to the strong recombination affecting of the auroral $[\text{O III}] \lambda 4363$ line. Although, our analysis is based on the $T_e([\text{S III}])$, the diagnostic that may not be much affected by strong recombination emission. The atomic databases may also be responsible for this discrepancy. In particular, for NGC 7009 and NGC 6778, SATELLITE used the atomic databases (PYNEB_18_01) while Jones et al. (2016) used the CHIANTI database⁸. Morisset et al. (2020) discuss the effect of different atomic data in the calculations of nebular parameters with an agreement of the order of 10 percent in the temperature sensitive line ratios and of 0.3 dex in chemical abundances (1D analysis).

Besides extended PNe, the SATELLITE code is also applicable to galaxies and H II regions observed with any IFU as well as to the emission line maps obtained from 3D photo-ionization models such as the MOCASSIN code (Ercolano et al. 2003, 2005) or the pseudo-3D models using the CLOUDY code (Ferland et al. 2013, 2017) and the PYTHON library PYCLOUDY (Morisset 2013). A full spectroscopic analysis of a source with all four models is doable in a day depending on the IFU and the size of the maps (number of spaxels.)

6.1 Future implementations

Further modules are planned to be implemented in the future version of SATELLITE.

- Faint collisionally excited lines as well as recombination lines,

⁸ <https://www.chiantidatabase.org/>

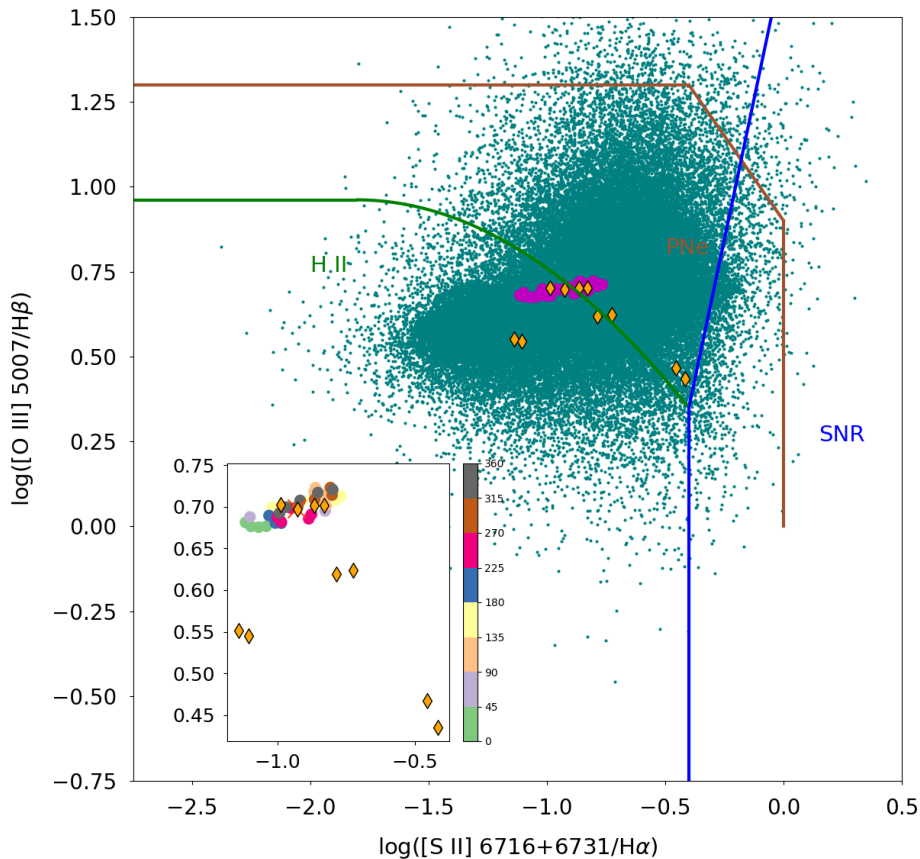


Figure 20. $\text{Log}([\text{S II}] 6716+6731/\text{H}\alpha)$ versus $\text{Log}([\text{O III}] 5007 \text{ \AA}/\text{H}\beta)$ diagnostic diagram of NGC 6778 as a representative example. The symbols are the same as in Fig. 11. The PNe, HII and SNRs zones are defined in Frew & Parker (2010); Sabin et al. (2013).

which may affect collisional lines sensitive to T_e and N_e measurements (such as $[\text{O III}] 4363$ and $[\text{N II}] 5755 \text{ \AA}$).

- Chemical abundances will also be calculated from the recombination lines as well as the corresponding abundance discrepancy factor (ADF) for all the modules.

- A new module for non-rectangular regions (e.g. pseudo-slit) or complex regions/list of spaxels based on the flux/intensity of particular emission lines or line ratios will be included.

- Strong line methods for the determination of chemical abundances.

- The Voronoi tessellation method so that the `SATELLITE` code will be able to provide maps of emission line and physical parameters through an automatic segmentation based on the signal-to-noise ratio (Vavilova et al. 2021). This method will make possible the investigation of the faint halos around PNe (Walsh et al. 2018).

- The publicly available grid of photo-ionization (`CLOUDY`) and shock models (`MAPPINGS`) from the Mexican Million Models database (3MdB, Morisset et al. 2015; Alarie & Morisset 2019) will be employed in order to construct more general emission line diagnostic diagrams (e.g. Akras et al. 2020a) and explore the contribution of each mechanism (photo-ionization and shocks).

- Principal component analysis tomography (PCA) technique will also be implemented to explore the variance in the emission of the

observed source and reduce the dimensionality of the maps without losing much information.

- Near-infrared wavelengths are also planned to be implemented for the spectroscopic analysis of data from IFUs such as the Gemini-North’s Near-Infrared Integral Field Spectrometer (NIFS@Gemini), the Spectrograph for INtegral Field Observations in the Near Infrared (SINFONI@VLT), the inFRared Imager and Dissector for Adaptive optics (FRIDA@GTC), or the upcoming NIRSpec unit on the James Webb Space Telescope (JWST), the GMT integral field spectrograph (GMTIFS) among others.

ACKNOWLEDGEMENTS

This paper is based on observations made with ESO Telescopes at the Paranal Observatory under Science Verification (SV) observing proposal 60.A-9347(A) and program ID 097.D-0241. SA acknowledges support under the grant 5077 financed by IAASARS/NOA. JG-R acknowledges support from the Severo Ochoa excellence program CEX2019-000920-S, from the State Research Agency (AEI) of the Spanish Ministry of Science, Innovation and Universities (MCIU) and the European Regional Development Fund (FEDER) under grant AYA2017-83383-P and from the Canarian Agency for Research, Innovation and Information Society (ACIISI), of the Ca-

Table 7. Statistical results of NGC 6778 MUSE datacube

Parameter	Num. of pix.	5% value	25% value	50% value	75% value	95% value	mean	SD
c(H β)	71074	0.11	0.43	0.61	0.67	1.21	0.60	0.31
Te(NII6548_84)_Ne(SII6716_31)	30383	7500	8290	9230	10900	21400	11000	4270
Ne(SII6716_31)_Te(NII6548_84)	35933	72	234	376	574	1760	582	571
Te(SIII6312_9069)_Ne(SII6716_31)	25306	6830	7970	8490	9590	19500	10000	3820
Ne(SII6716_31)_Te(SIII6312_9069)	25306	120	231	350	527	1070	488	550
Te(SIII6312_9069)_Ne(CIII5517_38)	13294	6950	7980	8340	8720	17300	9340	3220
Ne(CIII5517_38)_Te(SIII6312_9069)	13294	325	970	1770	2970	9280	2790	2700
abundance (He I 5876Å)	25170	0.131	0.158	0.163	0.167	0.202	0.165	0.029
abundance (He I 6678Å)	24921	0.122	0.159	0.164	0.170	0.245	0.173	0.054
abundance (He II 4686Å)	21188	1.92e-04	6.62e-04	1.98e-03	4.42e-03	1.75e-02	5.07e-03	1.05e-02
abundance ([O I] 6300 Å)	23444	1.29e-06	4.52e-06	1.19e-05	2.40e-05	7.83e-05	2.32e-05	3.53e-05
abundance ([O II] 7320 Å)	24296	6.44e-06	7.08e-05	1.90e-04	2.62e-04	8.46e-04	2.89e-04	5.60e-04
abundance ([O II] 7330 Å)	24402	9.38e-06	7.70e-05	1.93e-04	2.64e-04	9.32e-04	3.08e-04	6.25e-04
abundance ([O III] 4959 Å)	25304	2.72e-05	1.47e-04	3.09e-04	3.74e-04	7.05e-04	3.18e-04	2.71e-04
abundance ([O III] 5007 Å)	25304	2.69e-05	1.45e-04	3.06e-04	3.70e-04	6.96e-04	3.14e-04	2.68e-04
abundance ([N I] 5199 Å)	23377	1.29e-06	3.73e-06	7.75e-06	1.39e-05	4.08e-05	1.32e-05	1.76e-05
abundance ([N II] 5755 Å)	23625	7.19e-06	3.68e-05	7.81e-05	1.24e-04	3.17e-04	1.20e-04	1.21e-04
abundance ([N II] 6548 Å)	25052	8.34e-06	2.68e-05	5.75e-05	1.02e-04	2.51e-04	8.50e-05	7.80e-05
abundance ([N II] 6584 Å)	25052	8.88e-06	2.77e-05	5.94e-05	1.05e-04	2.57e-04	8.75e-05	8.00e-05
abundance ([S II] 6717 Å)	25306	2.38e-07	6.52e-07	1.28e-06	2.18e-06	5.42e-06	1.87e-06	1.75e-06
abundance ([S III] 6312 Å)	25306	1.26e-06	3.53e-06	5.31e-06	6.67e-06	9.72e-06	5.42e-06	2.77e-06
abundance ([Cl III] 5517 Å)	22910	6.51e-08	1.12e-07	1.57e-07	2.19e-07	7.53e-07	2.50e-07	3.19e-07
abundance ([Cl III] 5538 Å)	22415	7.16e-08	1.25e-07	1.77e-07	2.59e-07	9.30e-07	2.98e-07	3.93e-07
abundance ([Ar III] 7136 Å)	25268	3.83e-07	1.31e-06	2.03e-06	2.61e-06	3.97e-06	2.11e-06	1.23e-06
log(He I 5876/H α)	66912	-1.30	-1.11	-1.08	-0.96	-0.50	-0.99	0.34
log(He II 4686/H β)	52019	-2.40	-1.48	-0.79	-0.34	0.35	-0.88	0.84
log(He I 5876/He II 4686)	48946	-0.67	-0.16	0.29	0.76	1.79	0.38	0.92
log([N II] 6584/H α)	71496	-0.63	-0.33	-0.75	0.05	0.35	-0.12	0.30
log((([N II] 6548,6584)/[N II] 5755))	56399	0.62	1.10	1.65	2.02	2.26	1.56	0.63
log((([N II] 6548,6584)/([O III] 4959,5007)))	71047	-0.79	-0.56	-0.35	-0.20	0.16	-0.37	0.65
log([N I] 5200/H β)	56165	-2.06	-1.44	-0.92	-0.55	0.11	-0.95	0.67
log((([S II] 6716,6731)/H α))	65251	-1.40	-1.09	-0.80	-0.64	-0.35	-0.84	0.33
log([S II] 6716/[S II] 6731)	65250	-0.37	-0.05	0.04	0.10	0.38	0.03	0.23
log((([S II] 6716,6731)/([S III] 6312,9069)))	45420	-0.30	-0.11	0.81	0.23	0.54	0.09	0.27
log([O I] 6300/H α)	58687	-2.59	-1.80	-1.31	-0.99	-0.42	-1.38	0.67
log((([O I] 6300,6363)/([O III] 4959,5007)))	46717	-2.69	-1.99	-1.51	-1.21	-0.63	-1.58	0.76
log((([O I] 6300,6363)/([O II] 7320,7330)))	37067	-0.45	-0.04	0.21	0.39	0.71	0.18	0.35
log([O III] 5007/H β)	71309	0.42	0.58	0.68	0.75	1.05	0.70	0.19
log((([O II] 7320,7330)/([O III] 4959,5007)))	53580	-2.42	-2.23	-1.86	-1.41	-0.79	-1.77	0.86
log((([Cl III] 5517,5538)/H β))	44263	-2.04	-1.81	-0.97	-0.39	0.25	-0.99	0.81
log([Cl III] 5517/[Cl III] 5538)	44355	-0.49	-0.14	0.05	0.16	0.53	0.03	0.31

50% percentile corresponds to the median.

nary Islands Government, and the European Regional Development Fund (ERDF), under grant with reference ProID2021010074. DGR acknowledges support from the CNPq grants 428330/2018-5 and 313016/2020-8. JG-R, DJ, and RC acknowledge support under grant P/308614 financed by funds transferred from the Spanish Ministry of Science, Innovation and Universities, charged to the General State Budgets and with funds transferred from the General Budgets of the Autonomous Community of the Canary Islands by the MCIU. DJ also acknowledges support from the Erasmus+ programme of the European Union under grant number 2020-1-CZ01-KA203-078200. This study was also financed in part by the Coordenação de Aperfeiçoamento de Pessoal de Nível Superior - Brasil (CAPES) - Finance Code 001 (IA). CM acknowledges support from grant UNAM / PA-PIIT - IN101220. The following software packages in Python were used: Matplotlib (Hunter 2007), NumPy (Van der Walt et al. 2011),

SciPy (Virtanen et al. 2020), seaborn (Waskom 2021), and AstroPy (Astropy Collaboration et al. 2013, 2018).

DATA AVAILABILITY

The MUSE SV data underlying this article are available at the ESO online Archive (<http://archive.eso.org/cms.html>). The SATELLITE CODE, along with its documentation and examples, is available from the GitHub repository [<https://github.com/StavrosAkras/SATELLITE.git>].

REFERENCES

Acker A., Marcout J., Ochsenbein F., Stenholm B., Tylenda R., Schohn C.,

- 1992, The Strasbourg-ESO Catalogue of Galactic Planetary Nebulae. Parts I, II.
- Akras S., Gonçalves D. R., 2016, *MNRAS*, **455**, 930
- Akras S., Monteiro H., Aleman I., Farias M. A. F., May D., Pereira C. B., 2020a, *MNRAS*, **493**, 2238
- Akras S., Gonçalves D. R., Ramos-Larios G., Aleman I., 2020b, *MNRAS*, **493**, 3800
- Akras S., Monteiro H., Walsh J., Isabel A., Gonçalves D. R., Boumis P., 2022, *Galaxies*, **10**, 27
- Alarie A., Morisset C., 2019, *Rev. Mex. Astron. Astrofis.*, **55**, 377
- Ali A., Dopita M. A., 2019, *MNRAS*, **484**, 3251
- Ali A., Dopita M. A., Basurah H. M., Amer M. A., Alsulami R., Alruhaili A., 2016, *MNRAS*, **462**, 1393
- Allington-Smith J., Gerssen J., Robertson D., 2006, *New Astron. Rev.*, **50**, 235
- Astropy Collaboration et al., 2013, *A&A*, **558**, A33
- Astropy Collaboration et al., 2018, *AJ*, **156**, 123
- Bacon R., et al., 2010, in *Ground-based and Airborne Instrumentation for Astronomy III*, p. 773508, doi:10.1117/12.856027
- Baldwin J. A., Phillips M. M., Terlevich R., 1981, *PASP*, **93**, 5
- Burton M. G., Bulmer M., Moorhouse A., Geballe T. R., Brand P. W. J. L., 1992, *MNRAS*, **257**, 1P
- Cardelli J. A., Clayton G. C., Mathis J. S., 1989, *ApJ*, **345**, 245
- Delgado-Inglada G., Morisset C., Stasińska G., 2014, *MNRAS*, **440**, 536
- Dufour R. J., Kwitter K. B., Shaw R. A., Henry R. B. C., Balick B., Corradi R. L. M., 2015, *ApJ*, **803**, 23
- Ercolano B., Barlow M. J., Storey P. J., Liu X. W., 2003, *MNRAS*, **340**, 1136
- Ercolano B., Barlow M. J., Storey P. J., 2005, *MNRAS*, **362**, 1038
- Ercolano B., Dale J. E., Gritschneider M., Westmoquette M., 2012, *MNRAS*, **420**, 141
- Fang X., Liu X. W., 2011, *MNRAS*, **415**, 181
- Fang X., Liu X. W., 2013, *MNRAS*, **429**, 2791
- Ferland G. J., et al., 2013, *Rev. Mex. Astron. Astrofis.*, **49**, 137
- Ferland G. J., et al., 2017, *Rev. Mex. Astron. Astrofis.*, **53**, 385
- Frew D. J., Parker Q. A., 2010, *Publ. Astron. Soc. Australia*, **27**, 129
- García-Rojas J., Corradi R. L. M., Monteiro H., Jones D., Rodríguez-Gil P., Cabrera-Lavers A., 2016, *ApJ*, **824**, L27
- García-Rojas J., Morisset C., Jones D., Wesson R., Boffin H. M. J., Monteiro H., Corradi R. L. M., Rodríguez-Gil P., 2022, *MNRAS*, **510**, 5444
- Gómez-Llanos V., Morisset C., García-Rojas J., Jones D., Wesson R., Corradi R. L. M., Boffin H. M. J., 2020, *MNRAS*, **498**, L82
- Gonçalves D. R., Corradi R. L. M., Mampaso A., Perinotto M., 2003, *ApJ*, **597**, 975
- Gonçalves D. R., Ercolano B., Carnero A., Mampaso A., Corradi R. L. M., 2006, *MNRAS*, **365**, 1039
- Gonçalves D. R., Mampaso A., Corradi R. L. M., Quireza C., 2009, *MNRAS*, **398**, 2166
- Guerrero M. A., Miranda L. F., 2012, *A&A*, **539**, A47
- Guerrero M. A., Gruendl R. A., Chu Y. H., 2002, *A&A*, **387**, L1
- Howarth I. D., 1983, *MNRAS*, **203**, 301
- Hunter J. D., 2007, *Computing In Science & Engineering*, **9**, 90
- Jacoby G. H., Quigley R. J., Africano J. L., 1987, *PASP*, **99**, 672
- Jones D., Wesson R., García-Rojas J., Corradi R. L. M., Boffin H. M. J., 2016, *MNRAS*, **455**, 3263
- Kingsburgh R. L., Barlow M. J., 1994, *MNRAS*, **271**, 257
- Lame N. J., Pogge R. W., 1994, *AJ*, **108**, 1860
- Lame N. J., Pogge R. W., 1996, *AJ*, **111**, 2320
- Leal-Ferreira M. L., Gonçalves D. R., Monteiro H., Richards J. W., 2011, *MNRAS*, **411**, 1395
- Liu X. W., Barlow M. J., Danziger I. J., Clegg R. E. S., 1995, *MNRAS*, **273**, 47
- Luridiana V., Morisset C., Shaw R. A., 2015, *A&A*, **573**, A42
- Mediavilla E., Arribas S., Roth M., Cepa-Nogué J., Sánchez F., 2011, *3D Spectroscopy in Astronomy*
- Mendoza C., Zeippen C. J., 1982, *MNRAS*, **199**, 1025
- Miszalski B., Jones D., Rodríguez-Gil P., Boffin H. M. J., Corradi R. L. M., Santander-García M., 2011, *A&A*, **531**, A158
- Monreal-Ibero A., Walsh J. R., 2020, *A&A*, **634**, A47
- Monteiro H., Schwarz H. E., Gruenwald R., Heathcote S., 2004, *ApJ*, **609**, 194
- Monteiro H., Schwarz H. E., Gruenwald R., Guenther K., Heathcote S. R., 2005, *ApJ*, **620**, 321
- Monteiro H., Gonçalves D. R., Leal-Ferreira M. L., Corradi R. L. M., 2013, *A&A*, **560**, A102
- Morisset C., 2013, pyCloudy: Tools to manage astronomical Cloudy photoionization code (ascl:1304.020)
- Morisset C., 2018, in *Walking the Line 2018*, p. 2, doi:10.5281/zenodo.1206115
- Morisset C., Delgado-Inglada G., Flores-Fajardo N., 2015, *Rev. Mex. Astron. Astrofis.*, **51**, 103
- Morisset C., Luridiana V., García-Rojas J., Gómez-Llanos V., Bautista M., Mendoza Claudio 2020, *Atoms*, **8**, 66
- Phillips J. P., Cuesta L. C., Ramos-Larios G., 2010, *MNRAS*, **409**, 881
- Riesgo H., López J. A., 2006, *Rev. Mex. Astron. Astrofis.*, **42**, 47
- Rodríguez L. F., Gómez Y., 2007, *Rev. Mex. Astron. Astrofis.*, **43**, 173
- Rubin R. H., et al., 2002, *MNRAS*, **334**, 777
- Sabbadin F., Minello S., Bianchini A., 1977, *A&A*, **60**, 147
- Sabbadin F., Turatto M., Cappellaro E., Benetti S., Ragazzoni R., 2004, *A&A*, **416**, 955
- Sabin L., et al., 2013, *MNRAS*, **431**, 279
- Seaton M. J., 1979, *MNRAS*, **187**, 73
- Steffen W., Espíndola M., Martínez S., Koning N., 2009, *Rev. Mex. Astron. Astrofis.*, **45**, 143
- Sutherland R. S., Dopita M. A., 2017, *ApJS*, **229**, 34
- Sutherland R., Dopita M., Binette L., Groves B., 2018, MAPPINGS V: Astrophysical plasma modeling code (ascl:1807.005)
- Tsamis Y. G., Walsh J. R., Péquignot D., Barlow M. J., Danziger I. J., Liu X. W., 2008, *MNRAS*, **386**, 22
- Van der Walt S., Colbert S. C., Varoquaux G., 2011, *Computing in Science Engineering*, **13**, 22
- Vavilova I., Elyiv A., Dobrycheva D., Melnyk O., 2021, in *Zelinka I., Brescia M., Baron D., eds., Vol. 39, Intelligent Astrophysics*, pp 57–79, doi:10.1007/978-3-030-65867-0_3
- Veilleux S., Osterbrock D. E., 1987, *ApJS*, **63**, 295
- Virtanen P., et al., 2020, *Nature Methods*, **17**, 261
- Walsh J. R., Monreal-Ibero A., Barlow M. J., Ueta T., Wesson R., Zijlstra A. A., 2016, *A&A*, **588**, A106
- Walsh J. R., et al., 2018, *A&A*, **620**, A169
- Waskom M. L., 2021, *Journal of Open Source Software*, **6**, 3021

This paper has been typeset from a $\text{\TeX}/\text{\LaTeX}$ file prepared by the author.